

Magnetic interactions and possible structural distortion in kagome FeGe from first-principles study and symmetry analysis

Hanjing Zhou,^{1,2,*} Songsong Yan,^{1,2,*} Dongze Fan,^{1,2} Di Wang,^{1,2,†} and Xiangang Wan^{1,2}

¹*National Laboratory of Solid State Microstructures and School of Physics, Nanjing University, Nanjing 210093, China*

²*Collaborative Innovation Center of Advanced Microstructures, Nanjing University, Nanjing 210093, China*

(Dated: November 29, 2022)

Recently, charge density wave (CDW) order has been discovered in a magnetic kagome metal FeGe, providing a new platform to explore the possible connection between magnetism and CDW in a kagome lattice. Based on density functional theory and symmetry analysis, we present a comprehensive investigation of electronic structure, magnetic properties and possible structural distortion of FeGe. We estimate the magnetic parameters including Heisenberg and Dzyaloshinskii-Moriya (DM) interactions, and find that the ferromagnetic nearest-neighbor J_1 dominates over the others, while the magnetic interactions between nearest kagome layers favors antiferromagnetic. The Néel temperature T_N and Curie-Weiss temperature θ_{CW} are successfully reproduced, and the calculated magnetic anisotropy energy is also in consistent with the experiment. However, these reasonable Heisenberg interactions and magnetic anisotropy cannot explain the double cone magnetic transition, and the DM interactions, which even exist in the centrosymmetric materials, can result in this small magnetic cone angle. Unfortunately, due to the crystal symmetry of the high-temperature structure, the net contribution of DM interactions to double cone magnetic structure is absent. Based on the experimental $2 \times 2 \times 2$ supercell, we thus explore the subgroups of the parent phase. Group theoretical analysis reveals that there are 68 different distortions, and only four of them (space group $P622$ or $P6_322$) without inversion and mirror symmetry thus can explain the low-temperature magnetic structure. Furthermore, we suggest that these four proposed CDW phases can be identified by using Raman spectroscopy. Since DM interactions are very sensitive to small atomic displacements and symmetry restrictions, we believe that symmetry analysis is an effective method to reveal the interplay of delicate structural distortions and complex magnetic configurations.

I. INTRODUCTION

Kagome lattices are emerging as an exciting platform for the rich emergent physics, including magnetism, charge density wave (CDW), topology, and superconductivity [1–43]. Three key features have been identified in the electronic structure associated with its lattice geometry, which are flat band derived from the destructive phase interference of nearest-neighbour hopping, topological Dirac crossing at K point in the Brillouin zone (BZ), and a pair of van Hove singularities (vHSs) at M point [2–5]. When large density of states from the kagome flat bands are located near the Fermi level, strong electron correlations can induce magnetic order [2, 3]. There are several magnetic kagome materials, such as FeSn [6–10], Fe₃Sn₂ [11–14], Mn₃Sn [15], Co₃Sn₂S₂ [16] and AMn₆Sn₆ (A=Tb, Y) [17, 18], which usually exhibit magnetic order with ferromagnetically ordered layers that are either ferromagnetically or antiferromagnetically stacked. Meanwhile, when vHSs are located near the Fermi level, interaction between the saddle points and lattice instability could induce symmetry-breaking CDW order [4, 5], such as the class of recently discovered kagome materials AV₃Sb₅ (A=K, Rb, Cs) [19–41]. Significant interests have been focused on them since an unusual competition between unconventional superconductivity and CDW or-

der has been found [19–41]. Note that in kagome system, magnetic order and CDW order have not been usually observed simultaneously within one material, probably due to the fact that they originate from the flat band and the vHSs respectively, which have the large energy difference and usually do not both appear near the Fermi level [44].

Very recently, a CDW order has been discovered to appear deeply in a magnetically ordered kagome metal FeGe, providing the opportunity for understanding the interplay between CDW and magnetism in a kagome lattice [44–49]. Isostructural to FeSn [6–10] and CoSn [42, 43], hexagonal FeGe consists of stacks of Fe kagome planes with both in-plane and inter-plane Ge atoms [50]. A sequence of magnetic phase transitions have been discussed in 1970-80s [51–56]. Below $T_N = 410$ K, FeGe exhibits collinear A-type antiferromagnetic (AFM) order with moments aligned ferromagnetically (FM) within each plane and anti-aligned between layers, and becomes a c-axis double cone AFM structure at a lower temperature $T_{canting} = 60$ K [55, 56]. Recent neutron scattering, spectroscopy and transport measurements suggest a CDW in FeGe which takes place at T_{CDW} around 100K, providing the first example of a CDW in a kagome magnet [45, 46]. The CDW in FeGe enhances the AFM ordered moment and induces an emergent anomalous Hall effect (AHE) possibly associated with a chiral flux phase similar with AV₃Sb₅ [34–36], suggesting an intimate correlation between spin, charge, and lattice degree of freedom [45]. Though AHE is not usually seen in antiferro-

* These authors contributed equally to this work.

† Corresponding author: diwang0214@nju.edu.cn

magnets in zero field, recent studies have shown that a breaking of combined time-reversal and lattice symmetries in the antiferromagnetic state results in the AHE [57–59]. In kagome FeGe, the AHE associated with CDW order indicates that, the combined symmetry breaking occurs via the structural distortion or magnetic structure transition below the CDW temperature. The CDW in FeGe was then extensively studied experimentally and theoretically [44–49], and the CDW wavevectors are identical to that of AV_3Sb_5 [23–28]. However, sharply different from AV_3Sb_5 [39–41], all the theoretically calculated phonon frequencies in FeGe remain positive [44, 48, 49], and the structural distortion of the CDW phase remain elusive. It is firstly suggested to be reduced to $P622$ with the distortion of two non-equivalent Fe atoms [45], while the later works propose that FeGe shares the same space group of $P6/mmm$ with the pristine phase [48, 49]. Based on first-principles calculations and scanning tunneling microscopy, Shao *et al.* show that the CDW phase of FeGe exhibits a generalized Kekulé distortion [60] in the Ge honeycomb atomic layers [48]. Meanwhile, using hard x-ray diffraction and spectroscopy, Miao *et al.* report an experimental discovery of charge dimerization that coexists with the CDW phase in FeGe [49]. Therefore, the understanding of the magnetism, and the intertwined connection between complex magnetism and structural distortion in kagome FeGe is an emergency issue, which we will address in this work based on first-principles study and symmetry analysis.

In this work, we systematically analyze the electronic and magnetic properties of kagome FeGe. Our numerical results show that this material is a magnetic metal exhibiting large magnetic splitting around 1.8 eV. Based on combining magnetic force theorem and linear-response approach [61–63], the magnetic exchange parameters have been estimated. The results show that the nearest-neighbor J_1 is FM and dominates over the others, while the magnetic interactions between nearest kagome layers favors AFM, consequently resulting in the A-type AFM ground-state configuration. Based on these spin exchange parameters, the calculated Néel temperature and Curie-Weiss temperature also agree well with the experiments. Using the method in Ref. [64, 65], we also calculate the magnetic anisotropic energy (MAE) to be around 0.066 meV per Fe atom with easy axis being out of the kagome layers, which is in reasonable agreement with the experimental results [56]. However, the double cone magnetic transition at $T_{\text{canting}} = 60$ K cannot be reproduced by these reasonable magnetic parameters. We find that Dzyaloshinskii-Moriya (DM) interactions [66, 67] are much more efficient than Heisenberg interactions for causing this canted spin structure. Unfortunately, the space group $P6/mmm$ of high-temperature phase in FeGe has inversion symmetry and mirror symmetries, and all of them eliminate the net contribution of DM interactions to the double cone magnetic structure. It is well known that DM interactions are very sensitive to atomic displacements, while small structural

distortion usually has little effect on Heisenberg interactions. Therefore we explore the possible CDW distortions which can explain the low-temperature magnetic structure. Symmetry theoretical analysis reveals that there are 68 different distortions, which are the subgroups of the parent $P6/mmm$ phase with $2 \times 2 \times 2$ supercell [45, 46, 48, 49]. Based on the group theoretical analysis, we find that only four structures (space groups $P622$ and $P6_322$) without inversion and mirror symmetry thus can have double cone spin structure. We further propose that using Raman spectroscopy, these four CDW phases can be identified from their different numbers of Raman active peaks.

II. METHOD

The first-principles calculations have been carried out by using the full potential linearized augmented plane-wave method as implemented in the Wien2k package [68]. The converged k-point Monkhorst-Pack meshes are used for the calculations depending on materials. The self-consistent calculations are considered to be converged when the difference in the total energy of the crystal does not exceed $0.01 mRy$. We adopt local spin-density approximation (LSDA) [69] as the exchange-correlation potential, and include the spin orbit coupling (SOC) using the second-order variational procedure [70].

The spin exchange interactions, including Heisenberg and DM interactions [66, 67], are calculated using first principles based on combining magnetic force theorem and linear-response approach [61–63], which have successfully applied to various magnetic materials [62, 63, 71–73].

Monte Carlo (MC) simulations are performed with Metropolis algorithm for Heisenberg model [74–76]. The size of the cell in the MC simulation are $16 \times 16 \times 16$ -unit cells with periodic boundary conditions. At each temperature we carry out 400000 sweeps to prepare the system, and sample averages are accumulated over 800000 sweeps.

III. RESULTS

A. The electronic and magnetic properties

The pristine phase of FeGe crystallizes in the hexagonal structure with space group $P6/mmm$ (No. 191) [50], where the coordinates of the atoms are shown in table II and Fig. 1. Firstly we perform nonmagnetic local-density approximation (LDA) + SOC calculation, and show the band structures in Fig. 2(a). While Ge- $2p$ states are mainly located between -6.0 and -2.0 eV, the main contribution around the Fermi level comes from the $3d$ orbitals of Fe ions, as shown in Fig. 4 of Appendix. Consistent with previous first-principle calculations [44, 47], the kagome flat bands around the Fermi level exhibit a large

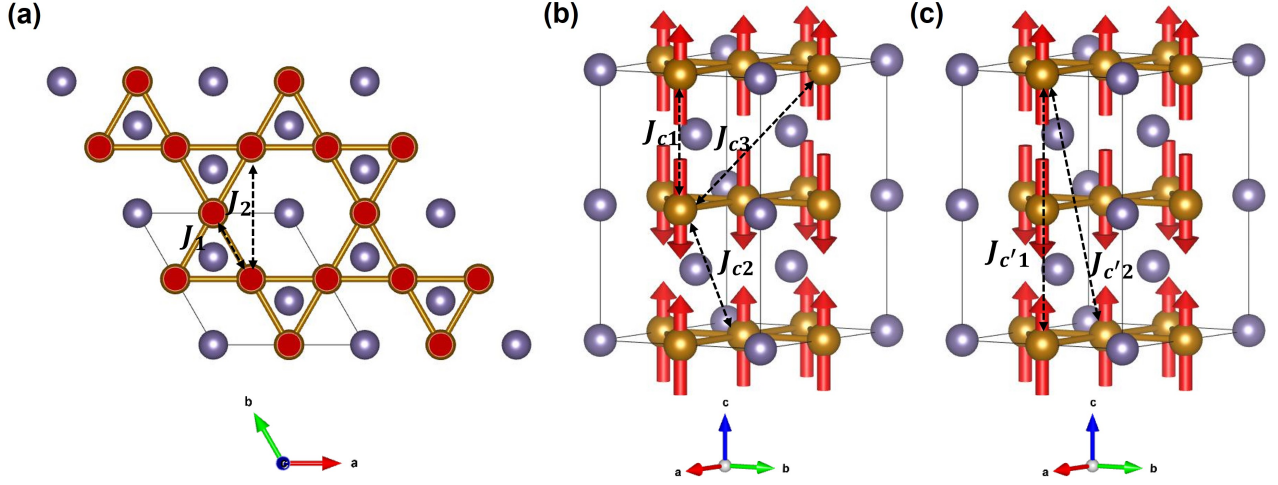


FIG. 1. Crystal and magnetic structures of FeGe. Yellow and purple spheres represent Fe and Ge atoms respectively, while arrows denote magnetic moments of Fe atoms. (a) Top view of FeGe. The exchange interactions J_i denote the i th-nearest-neighbor interactions between Fe ions within kagome layers. (b) The exchange interactions J_{ci} denote the i th-nearest-neighbor interactions between Fe ions on the nearest kagome layers. (c) The exchange interactions $J_{c'i}$ denote the i th-nearest-neighbor interactions between Fe ions on the next nearest kagome layers.

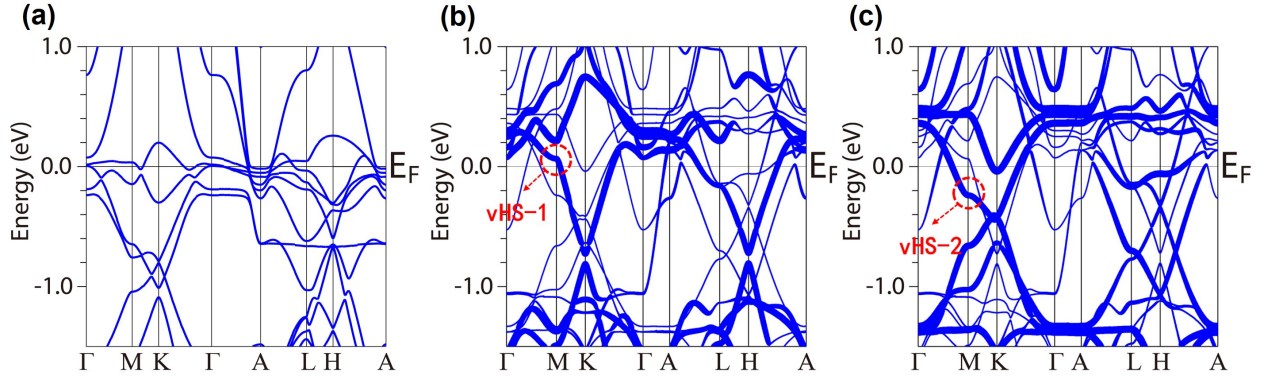


FIG. 2. (a) Band structure of nonmagnetic FeGe from LDA + SOC calculation. (b),(c) Orbital-resolved band structure of Fe- $d_{xy}/d_{x^2-y^2}$ and Fe- d_{xz}/d_{yz} for A-type AFM configuration with spin orientations along the (001) direction from LSDA + SOC calculation.

peak in the density of states, which indicates the magnetic instability. Therefore, LSDA + SOC calculations are performed based on the A-type AFM configuration and the band structures are shown in Figs. 2(b) and 2(c). The magnetic moment of Fe ions is estimated to be $1.55 \mu_B$, which is in agreement with the previous experimental value around $1.7 \mu_B$ [52, 54]. Note that each kagome layer is FM and the key signatures of electronic structures in kagome lattice are remained. The magnetic splitting is around 1.8 eV (see Fig. 4 of Appendix), which makes that the flat bands above and below Fermi level correspond to the spin minority bands and spin majority bands respectively. Meanwhile, the vHSs that are relatively far from the Fermi level in the nonmagnetic state, are brought near the Fermi level by the spin splitting, as

shown in Figs. 2(b) and 2(c). We present orbital-resolved band structures, and find that the vHSs near the Fermi level, which marked as vHS-1 and vHS-2 in Figs. 2(b) and 2(c), are mainly contributed by the $d_{xy}/d_{x^2-y^2}$ and d_{xz}/d_{yz} orbitals respectively. These vHSs near the Fermi level are suggested to induce symmetry-breaking CDW order in kagome metal FeGe [44].

To quantitatively understand the rich magnetic phenomenon in kagome FeGe, a microscopic magnetic model with proper parameters is extremely important. Based on the calculated electronic structures, we estimate the exchange parameters including Heisenberg and DM interactions using the linear-response approach [61–63] and summarize the results in table I. As shown in Fig. 1, we divide the magnetic interactions considered into three

TABLE I. Spin exchange parameters (in meV) including Heisenberg and DM interactions of FeGe evaluated from LSDA+SOC calculations, respectively. The Fe-Fe distances and the corresponding number of neighbors NN are presented in the second and third columns.

	Distance(Å)	NN	J	DM
J_1	2.50	4	-41.97	(0, 0, 0.03)
J_2	4.33	4	5.49	(0, 0, -0.12)
J_{c1}	4.05	2	8.44	(0, 0, 0)
J_{c2}	4.76	8	-2.04	(0.01, -0.02, -0.07)
J_{c3}	5.93	8	1.81	(0.07, -0.04, -0.09)
$J_{c'1}$	8.11	2	-0.66	(0, 0, 0)
$J_{c'2}$	8.49	8	0.09	(-0.04, -0.09, -0.03)

types: the exchange interactions J_i , J_{ci} and $J_{c'i}$ represent the i th-nearest-neighbor interactions between Fe ions within kagome layers, on the nearest kagome layers, and on the next nearest kagome layers respectively. As shown in table I, the in-plane nearest neighbor coupling J_1 favors FM order and is estimated to be -41.97 meV, which has the similar value with the one in kagome FeSn (around -50 meV) [7–10]. Note that the distance in J_1 is 2.5 Å while the others are all greater than 4 Å. Though there are also AFM in-plane magnetic interactions such as in-plane next-nearest neighbor coupling J_2 , they are at least an order of magnitude smaller than J_1 , resulting in each FM kagome layer. As the out-of-plane nearest neighbor coupling, J_{c1} is estimated to be 8.44 meV. It makes the magnetic moments stacked antiferromagnetically between kagome layers, consequently resulting in the A-type AFM order in kagome FeGe, which is consistent with the experiment [51]. It is worth mentioning that, SOC always exists and leads to the DM interactions even in the centrosymmetric compound FeGe, since not all Fe-Fe bonds have inversion symmetry. For the equivalent DM interactions connected by the crystal symmetry (see table III-V in Appendix), we only present one of them as a representative. As shown in table I, the in-plane nearest neighbor \mathbf{D}_1 has the form of (0, 0, D_1^z) according to the crystal symmetry, and D_1^z is estimated to be 0.03 meV. Meanwhile, the in-plane next nearest neighbor \mathbf{D}_2 is estimated to be (0, 0, -0.12) meV. For the out-of-plane nearest neighbor, \mathbf{D}_{c1} is zero because its bond has an inversion center. The other calculated DM interactions are also listed in table I, and most of them are small in the order of 0.01 meV.

To explore the magnetic anisotropy in kagome FeGe, we consider the MAE with the expression $E_{MAE} = K_2 \sin^2 \theta + K_4 \sin^4 \theta$ [51, 54–56] neglecting terms of order higher than four, where θ is the angle between the magnetic moment and the z-axis. The values of K_2 and K_4 are estimated to be 0.066 meV and 0.018 meV respectively based on the approach of Ref. [64, 65], which are in reasonable agreement with the experimental values 0.021 meV [56] and 0.012 meV [51]. Here K_2 and K_4 are both positive, making out-of-plane magnetization favored, which is different from the easy-plane anisotropy

in FeSn [8]. Note that positive K_4 is the requirement for the stability of the double cone magnetic structure, which will be discussed below.

According to the experiments [51], the Curie-Weiss temperature θ_{CW} in kagome FeGe is -200 K while the Néel temperature T_N is 410 K. The relative low value of the frustration index $|\theta_{CW}|/T_N$ (smaller than 1) reveals the interplay of the FM and AFM interactions [77]. As shown in table I, our calculated results of spin exchange couplings also verify the coexistence of the FM and AFM interactions. Based on these calculated spin exchange parameters, we calculate Néel temperature and Curie-Weiss temperature by MC simulations [74–76]. The θ_{CW} and T_N are calculated to be -219 K and 370 K respectively, which agrees well with the experiment [51].

Similar to the electronic structure of a kagome lattice, the spin wave for a localized spin model with FM nearest-neighbor magnetic exchange also yields a flat magnetic band and a Dirac magnon [78]. Using the calculated spin model parameters, one can obtain the magnon spectrum [79, 80]. The calculated spin-wave dispersion along the high-symmetry axis is shown in Fig. 3, which basically captures the key features of kagome lattice geometry. Similar with FeSn case [7–10], strongly dispersive magnons in the xy-plane extend to about 260 meV, where the magnon dispersion along the out-of-plane direction has relatively small bandwidth of less than 15 meV, reflecting the quasi-two-dimensional magnetic properties in kagome FeGe. Meanwhile, the Dirac-like node appears at the K point at about 107 meV, and we find that DM interactions introduce a gap around 1 meV at the Dirac point, as shown in the inset of Fig. 3. Furthermore, the single-ion anisotropy produces a spin gap of about 2 meV, which could be verified in future inelastic neutron scattering experiments.

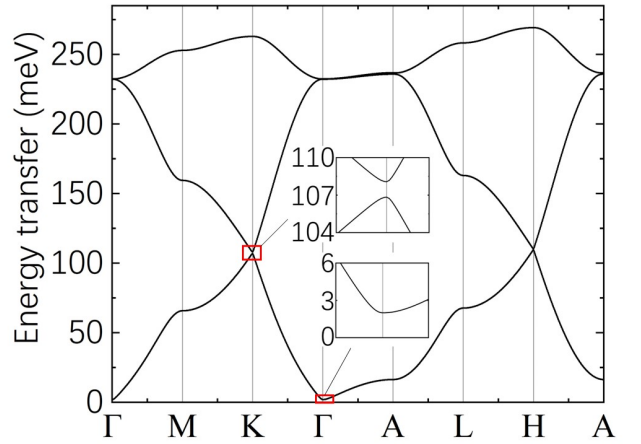


FIG. 3. Calculated spin-wave dispersion curves along the high-symmetry axis for FeGe. The insets show the spin gap at Γ point induced by easy-axis anisotropy, and the gap located at about 107 meV of K point induced by DM interactions.

B. The double cone magnetic structure

At $T_{\text{canting}} = 60$ K, the kagome lattice FeGe becomes a c-axis double cone AFM structure [51, 52, 54–56] where the magnetic ground state could be written as Eq. (10) in Appendix. Considering the magnetic interactions and the MAE, the total energy of the double cone spin structure could be written as Eq. (12) in Appendix. When DM interactions are not considered, the extremum condition of the total energy gives the equilibrium value of wave vector δ and the cone half angle θ (i.e. Eq. (13) and (14) in Appendix)

$$\cos \delta = \frac{\sum_i N_{ci} J_{ci}}{4 \sum_i N_{c'i} J_{c'i}} \quad (1)$$

$$\sin^2 \theta = -\frac{K_2 - \frac{1}{2N} \sum_i N_{c'i} J_{c'i} \delta^4}{2K_4} \quad (2)$$

Note that the minimum of the total energy requires that the second derivative of Eq. (12) in Appendix is positive, thus K_4 must be positive. Hence $K_2 - \frac{1}{2N} \sum_i N_{c'i} J_{c'i} \delta^4$ (i.e. the numerator of Eq. (2)) must be negative. However, our reasonable magnetic parameters cannot explain the double cone magnetic ground state. The value of wave vector δ is small in experimental measurement (0.17 in Ref. [51] and 0.25 in Ref. [53]), thus δ^4 is around 0.001. Meanwhile, the value of $\frac{1}{2N} \sum_i N_{c'i} J_{c'i}$ is of the order of 1 meV, which obviously cannot explain the double cone magnetic structure [51].

We thus consider the effect of DM interactions on double cone spin structure. Since the exchange interactions between two next nearest neighbor kagome layers are relatively small, we only consider the Heisenberg and DM interactions between two nearest neighbor kagome layers, i.e. J_{ci} and \mathbf{D}_{ci} . We find that wave vector δ and the cone half angle θ have the expressions as (i.e. Eq. (15) and (16) in Appendix)

$$\tan \delta = \frac{\sum_{i,j} D_{ci,j}^z}{\sum_i N_{ci} J_{ci}} \quad (3)$$

$$\sin^2 \theta = -\frac{K_2 - \frac{1}{2N} \sum_{i,j} D_{ci,j}^z \delta}{2K_4} \quad (4)$$

It should be noted that, comparing Eq. (2) and (4), DM interactions are more efficient than Heisenberg interactions for causing double cone spin structure since δ is small. Though the space group $P6/mmm$ of high-temperature phase in FeGe has a global inversion center, not all Fe-Fe bonds have inversion symmetry and DM interactions could exist. However, according to the inversion symmetry of space group $P6/mmm$, the total contribution of DM interactions to the energy of double cone magnetic structure in Eq. (12) is absent, i.e. $\sum_{i,j} D_{ci,j}^z = 0$ (see Appendix D). Meanwhile, mirror symmetries in space group $P6/mmm$ would also eliminate the contribution of DM interactions based on the

symmetry analysis. Therefore, DM interactions have no net contribution to double cone magnetic structure with the symmetry of high-temperature phase. For the CDW phases with the space group of $P6/mmm$ suggested by Ref. [48, 49] (the first two structures of the table VI in Appendix), the total contribution of DM interactions is still absent and cannot explain the magnetic ground state of double cone spin structure.

C. The interplay of CDW and double cone structure

As mentioned above, DM interactions play a more important role in the double cone spin structure. Meanwhile, it is very sensitive to atomic displacements. Therefore, in the following we explore the CDW phases with symmetry-allowed DM contribution to double cone spin structure which may explain the canted magnetic ground state.

The $2 \times 2 \times 2$ supercell structure of CDW phase (compared with the nonmagnetic pristine phase) is suggested experimentally [45, 46, 48, 49]. Considering all CDW phases whose associated point group in the maximal subgroups of D_{6h} , we find 68 different possible CDW phases which are the subgroups of the parent $P6/mmm$ phase with $2 \times 2 \times 2$ supercell (see details in Appendix D). The corresponding relations of atomic positions between the pristine phase and these proposed CDW phases are all summarized in table VI-X of Appendix.

Note that the inversion symmetry and mirror symmetries would all eliminate the net contribution of DM interactions as discussed above. We find that among these 68 proposed CDW phases, only four distorted structures break all these symmetries above, and can lead to non-zero DM contribution in Eq. (12) of Appendix. We list the corresponding Wyckoff positions (WP) and the coordinates of the atoms in the pristine phase and these four CDW phases in table II. They comes from two space groups $P622$ and $P6_322$. It should be mentioned that there are two different CDW phases for each of these two space groups, which are labeled as (type I) and (type II) in table II. Note that the CDW phase with $P622$ space group is also suggested in Ref. [45].

Raman spectroscopy is a fast and usually non-destructive technique which can be used to characterize the structural distortion of materials. Based on the atomic coordinates in table II, we predict the irreducible representation of the Raman active modes of these four proposed CDW phases using symmetry analysis [81]. For $P622$ (type I) and (type II) CDW phases, the Raman active modes are $8A_1 + 26E_1 + 22E_2$ and $10A_1 + 26E_1 + 22E_2$. Meanwhile, for $P6_322$ (type I) and (type II), the Raman active modes are $8A_1 + 24E_1 + 24E_2$ and $10A_1 + 24E_1 + 24E_2$, respectively. Note that even within the same symmetry of space group $P622$, the different structural distortion of CDW phases $P622$ (type I) and (type II) could result in the different number of Raman active

TABLE II. Four types of $2 \times 2 \times 2$ CDW phases which can lead to non-zero DM contribution to double cone spin structure. The corresponding Wyckoff positions and the coordinates of the atoms in the pristine phase and these four CDW phases are summarized.

Pristine phase($P6/mmm$)			$P622$ (type I)			$P622$ (type II)			$P6_322$ (type I)			$P6_322$ (type II)		
WP	Coordinates		WP	Coordinates		WP	Coordinates		WP	Coordinates		WP	Coordinates	
Ge1 1a	(0, 0, 0)		Ge1 1a	(0, 0, 0)		Ge1 2e	(0, 0, z_1)		Ge1 2a	(0, 0, 0)		Ge1 2b	(0, 0, $1/4$)	
			Ge2 1b	(0, 0, $1/2$)		Ge2 6i	($1/2$, 0, z_2)		Ge2 6g	(x_1 , 0, 0)		Ge2 6h	(x_1 , $2x_1$, $1/4$)	
			Ge3 3f	(0, $1/2$, 0)										
			Ge4 3g	(0, $1/2$, $1/2$)										
Ge2 2d	(1/3, 2/3, 1/2)		Ge5 4h	(1/3, 2/3, z_1)		Ge3 2c	(1/3, 2/3, 0)		Ge3 2c	(1/3, 2/3, $1/4$)		Ge3 4f	(1/3, 2/3, z_2)	
			Ge6 12n	(x_2 , y_2 , z_2)		Ge4 2d	(1/3, 2/3, $1/2$)		Ge4 2d	(1/3, 2/3, $3/4$)		Ge4 12i	(x_3 , y_3 , z_3)	
						Ge5 6l	(x_3 , $2x_3$, 0)		Ge5 6h	(x_2 , $2x_2$, $1/4$)				
						Ge6 6m	(x_4 , $2x_4$, $1/2$)		Ge6 6h	(x_3 , $2x_3$, $1/4$)				
Fe 3f	(1/2, 0, 0)		Fe1 6j	(x_3 , 0, 0)		Fe1 12n	(x_5 , y_5 , z_5)		Fe1 6g	(x_4 , 0, 0)		Fe1 6h	(x_4 , $2x_4$, $1/4$)	
			Fe2 6k	(x_4 , 0, $1/2$)		Fe2 12n	(x_6 , y_6 , z_6)		Fe2 6g	(x_5 , 0, 0)		Fe2 6h	(x_5 , $2x_5$, $1/4$)	
			Fe3 6l	(x_5 , $2x_5$, 0)					Fe3 12i	(x_6 , y_6 , z_6)		Fe3 12i	(x_6 , y_6 , z_6)	
			Fe4 6m	(x_6 , $2x_6$, $1/2$)										

modes (56 and 58 respectively), which could be identified by Raman spectroscopy.

IV. CONCLUSION

In conclusion, we systematically analyze the electronic and magnetic properties of kagome FeGe. Our numerical results show that this material is a magnetic metal exhibiting large magnetic splitting around 1.8 eV. The magnetic splitting makes the flat bands away from Fermi level, and bring two vHSs near the Fermi level. We estimate the magnetic parameters, and find that the ferromagnetic nearest-neighbor J_1 dominates over the others, while the magnetic interactions between nearest kagome layers favors antiferromagnetic. Based on these spin exchange parameters, the calculated Néel temperature and Curie-Weiss temperature also agree well with the experiments. Furthermore, the magnetic excitation spectra are calculated using linear spin wave theory and a spin gap about 2 meV is predicted. Note that the double cone magnetic transition at a lower temperature cannot be reproduced by these reasonable magnetic parameters. Meanwhile, due to the inversion symmetry and mirror symmetries in the space group $P6/mmm$ of high-temperature phase, the total contribution of DM interactions to the double cone magnetic structure is absent. Since DM interactions are very sensitive to small atomic displacements and symmetry restrictions, and also much more efficient than Heisenberg interactions for causing this canted spin structure, we propose that the double cone spin structure may arise from the structural distortion. We explore 68 possible CDW phases of kagome FeGe which are subgroups of the pristine phase with $2 \times 2 \times 2$ supercell, and symmetry-allowed four CDW structures which have non-zero DM contribution and may result in double cone spin structure are proposed. These four CDW phases belong to two space groups $P622$ and $P6_322$, and we further propose that they can

be identified from their different numbers of Raman active peaks. Therefore, we believe that symmetry analysis plays an important role in exploring the possible structural distortion in complex magnetic configurations.

V. ACKNOWLEDGEMENTS

This work was supported by the NSFC (No. 12188101, 11834006, 12004170, 11790311, 51721001), National Key R&D Program of China (No. 2018YFA0305704), Natural Science Foundation of Jiangsu Province, China (Grant No. BK20200326), and the excellent programme in Nanjing University. Xiangang Wan also acknowledges the support from the Tencent Foundation through the XPLORER PRIZE.

VI. APPENDIX

A. The density of states in kagome FeGe

The Partial density of states (DOS) of FeGe from LSDA + SOC calculations are shown in Fig. 4.

B. The symmetry restrictions on the magnetic interactions

Here we consider a general pairwise spin model

$$H = \sum_{l,n,l',n'} \mathbf{S}_{ln} \mathbf{J}_{\mathbf{R}_l + \boldsymbol{\tau}_n, \mathbf{R}_{l'} + \boldsymbol{\tau}_{n'}} \mathbf{S}_{l'n'} \quad (5)$$

where $\mathbf{J}_{\mathbf{R}_l + \boldsymbol{\tau}_n, \mathbf{R}_{l'} + \boldsymbol{\tau}_{n'}}$, a 3×3 tensor, represents the spin exchange parameters. \mathbf{R}_l and $\boldsymbol{\tau}_n$ represent the lattice translation vector and the position of magnetic ions in the lattice basis, and \mathbf{S}_{ln} means the spin at the site of $\mathbf{R}_l + \boldsymbol{\tau}_n$. Translation symmetry will restrict

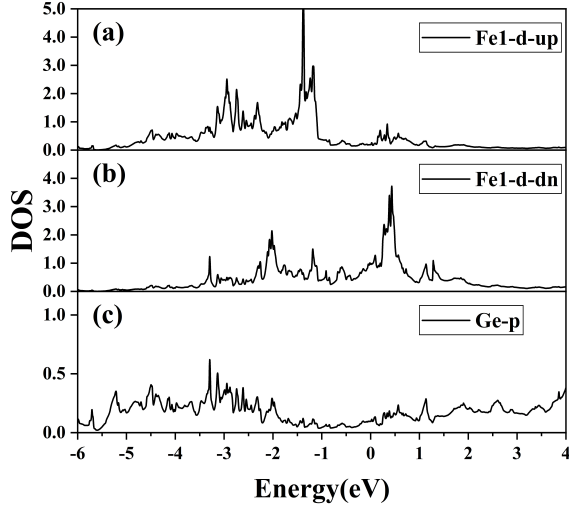


FIG. 4. Partial DOS of FeGe from LSDA + SOC calculations. The Fermi energy is set to zero. (a) and (b) represent the spin-up and spin-down channel of d orbitals in Fe1 atom located at $(1/2, 0, 0)$, while (c) represents the DOS of Ge- p orbitals.

TABLE III. The distances, the bond information and the symmetry restricted interactions of corresponding Fe ions within xy-planes. Here n, n' and R_l correspond to $\mathbf{J}_{\tau_n, \tau_{n'} + \mathbf{R}_l}$, where R_l and τ_n represent the lattice translation vector and the position of magnetic ions in the lattice basis. Three magnetic ions are located at $\tau_1 (1/2, 0, 0)$, $\tau_2 (0, 1/2, 0)$, and $\tau_3 (1/2, 1/2, 0)$. The equivalent \mathbf{D}_i 's are labeled as the sub-index of j , i.e. the $\mathbf{D}_{i,j}$ in the table.

Distance(Å)	n	n'	R_l	J	DM
2.50	3	1	(0,1,0)	J_1	$\mathbf{D}_{1,1}(0, 0, D_1^z)$
	1	2	(0,-1,0)	J_1	$\mathbf{D}_{1,2}(0, 0, D_1^z)$
	2	3	(0,0,0)	J_1	$\mathbf{D}_{1,3}(0, 0, D_1^z)$
	3	1	(0,0,0)	J_1	$\mathbf{D}_{1,4}(0, 0, D_1^z)$
	1	2	(1,0,0)	J_1	$\mathbf{D}_{1,5}(0, 0, D_1^z)$
	2	3	(-1,0,0)	J_1	$\mathbf{D}_{1,6}(0, 0, D_1^z)$
4.33	1	2	(1,-1,0)	J_2	$\mathbf{D}_{2,1}(0, 0, D_2^z)$
	2	3	(0,1,0)	J_2	$\mathbf{D}_{2,2}(0, 0, D_2^z)$
	3	1	(-1,0,0)	J_2	$\mathbf{D}_{2,3}(0, 0, D_2^z)$
	1	2	(0,0,0)	J_2	$\mathbf{D}_{2,4}(0, 0, D_2^z)$
	2	3	(-1,-1,0)	J_2	$\mathbf{D}_{2,5}(0, 0, D_2^z)$
	3	1	(1,1,0)	J_2	$\mathbf{D}_{2,6}(0, 0, D_2^z)$

$\mathbf{J}_{\mathbf{R}_l + \tau_n, \mathbf{R}_{l'} + \tau_{n'}}$ to be only related to $\mathbf{J}_{\tau_n, \tau_{n'} + \mathbf{R}_{l''}}$ where $\mathbf{R}_{l''} = \mathbf{R}_{l'} - \mathbf{R}_l$, irrespective of the starting unit cell. Other spatial symmetries will also give restrictions on the magnetic exchange interactions. We consider a general space group element $\{\alpha|\mathbf{t}\}$, where the left part represents the rotation and the right part means the lattice translation. Supposing under this symmetry operator, $\mathbf{R}_m + \tau_p$ and $\mathbf{R}_{m'} + \tau_{p'}$ transfer to $\mathbf{R}_l + \tau_n$ and $\mathbf{R}_{l'} + \tau_{n'}$, re-

TABLE IV. The distances, the bond information and the symmetry restricted interactions of corresponding Fe ions between nearest-neighbor (001)-planes. Here n, n' and R_l correspond to $\mathbf{J}_{\tau_n, \tau_{n'} + \mathbf{R}_l}$, where R_l and τ_n represent the lattice translation vector and the position of magnetic ions in the lattice basis. Three magnetic ions are located at $\tau_1 (1/2, 0, 0)$, $\tau_2 (0, 1/2, 0)$, and $\tau_3 (1/2, 1/2, 0)$. The equivalent \mathbf{D}_{ci} 's are labeled as the sub-index of j , i.e. the $\mathbf{D}_{ci,j}$ in the table.

Distance(Å)	n	n'	R_l	J	DM
4.05	1	1	(0,0,1)	J_{c1}	$\mathbf{D}_{c1,1}(0, 0, 0)$
	2	2	(0,0,1)	J_{c1}	$\mathbf{D}_{c1,2}(0, 0, 0)$
	3	3	(0,0,1)	J_{c1}	$\mathbf{D}_{c1,3}(0, 0, 0)$
4.76	3	1	(0,0,1)	J_{c2}	$\mathbf{D}_{c2,1}(D_{c2}^x, -\sqrt{3}D_{c2}^y, D_{c2}^z)$
	1	2	(1,0,1)	J_{c2}	$\mathbf{D}_{c2,2}(D_{c2}^x, \sqrt{3}D_{c2}^y, D_{c2}^z)$
	2	3	(-1,0,1)	J_{c2}	$\mathbf{D}_{c2,3}(-2D_{c2}^x, 0, D_{c2}^z)$
	3	1	(0,1,1)	J_{c2}	$\mathbf{D}_{c2,4}(-D_{c2}^x, \sqrt{3}D_{c2}^y, D_{c2}^z)$
	1	2	(0,-1,1)	J_{c2}	$\mathbf{D}_{c2,5}(-D_{c2}^x, -\sqrt{3}D_{c2}^y, D_{c2}^z)$
	2	3	(0,0,1)	J_{c2}	$\mathbf{D}_{c2,6}(2D_{c2}^x, 0, D_{c2}^z)$
	1	3	(0,-1,1)	J_{c2}	$\mathbf{D}_{c2,7}(-D_{c2}^x, \sqrt{3}D_{c2}^y, -D_{c2}^z)$
	2	1	(0,1,1)	J_{c2}	$\mathbf{D}_{c2,8}(-D_{c2}^x, -\sqrt{3}D_{c2}^y, -D_{c2}^z)$
	3	2	(0,0,1)	J_{c2}	$\mathbf{D}_{c2,9}(2D_{c2}^x, 0, -D_{c2}^z)$
	1	3	(0,0,1)	J_{c2}	$\mathbf{D}_{c2,10}(D_{c2}^x, -\sqrt{3}D_{c2}^y, -D_{c2}^z)$
	2	1	(-1,0,1)	J_{c2}	$\mathbf{D}_{c2,11}(D_{c2}^x, \sqrt{3}D_{c2}^y, -D_{c2}^z)$
	3	2	(1,0,1)	J_{c2}	$\mathbf{D}_{c2,12}(-2D_{c2}^x, 0, -D_{c2}^z)$
5.93	2	1	(-1,1,1)	J_{c3}	$\mathbf{D}_{c3,1}(-\sqrt{3}D_{c3}^x, D_{c3}^y, -D_{c3}^z)$
	3	2	(0,-1,1)	J_{c3}	$\mathbf{D}_{c3,2}(0, -2D_{c3}^y, -D_{c3}^z)$
	1	3	(1,0,1)	J_{c3}	$\mathbf{D}_{c3,3}(\sqrt{3}D_{c3}^x, D_{c3}^y, -D_{c3}^z)$
	2	1	(0,0,1)	J_{c3}	$\mathbf{D}_{c3,4}(\sqrt{3}D_{c3}^x, -D_{c3}^y, -D_{c3}^z)$
	3	2	(1,1,1)	J_{c3}	$\mathbf{D}_{c3,5}(0, 2D_{c3}^y, -D_{c3}^z)$
	1	3	(-1,-1,1)	J_{c3}	$\mathbf{D}_{c3,6}(-\sqrt{3}D_{c3}^x, -D_{c3}^y, -D_{c3}^z)$
	1	2	(0,0,1)	J_{c3}	$\mathbf{D}_{c3,7}(\sqrt{3}D_{c3}^x, -D_{c3}^y, D_{c3}^z)$
	2	3	(-1,-1,1)	J_{c3}	$\mathbf{D}_{c3,8}(0, 2D_{c3}^y, D_{c3}^z)$
	3	1	(1,1,1)	J_{c3}	$\mathbf{D}_{c3,9}(-\sqrt{3}D_{c3}^x, -D_{c3}^y, D_{c3}^z)$
	1	2	(1,-1,1)	J_{c3}	$\mathbf{D}_{c3,10}(-\sqrt{3}D_{c3}^x, D_{c3}^y, D_{c3}^z)$
	2	3	(0,1,1)	J_{c3}	$\mathbf{D}_{c3,11}(0, -2D_{c3}^y, D_{c3}^z)$
	3	1	(-1,0,1)	J_{c3}	$\mathbf{D}_{c3,12}(\sqrt{3}D_{c3}^x, D_{c3}^y, D_{c3}^z)$

spectively, meanwhile the transformation of spin becomes $\mathbf{S}_{mp} = M(\alpha)\mathbf{S}_{ln}$, where $M(\alpha)$ is the representation matrix of the proper rotation part of the operation α in the coordinate system, we get the following expression:

$$\begin{aligned}
H &= \sum_{l,n,l',n'} \mathbf{S}_{ln} \mathbf{J}_{\mathbf{R}_l + \tau_n, \mathbf{R}_{l'} + \tau_{n'}} \mathbf{S}_{l'n'} \\
&= \sum_{l,n,l',n'} \mathbf{S}_{ln} M^\dagger(\alpha) M(\alpha) \mathbf{J}_{\mathbf{R}_l + \tau_n, \mathbf{R}_{l'} + \tau_{n'}} M^\dagger(\alpha) M(\alpha) \mathbf{S}_{l'n'} \\
&= \sum_{m,p,m',p'} \mathbf{S}_{mp} [M(\alpha) \mathbf{J}_{\mathbf{R}_l + \tau_n, \mathbf{R}_{l'} + \tau_{n'}} M^\dagger(\alpha)] \mathbf{S}_{m'p'} \quad (6)
\end{aligned}$$

Then the exchange interactions should satisfy the following condition:

$$\mathbf{J}_{\mathbf{R}_m + \tau_p, \mathbf{R}_{m'} + \tau_{p'}} = M(\alpha) \mathbf{J}_{\mathbf{R}_l + \tau_n, \mathbf{R}_{l'} + \tau_{n'}} M^\dagger(\alpha) \quad (7)$$

After decomposing the 3×3 tensor \mathbf{J} into scalar Heisenberg term J and vector DM term \mathbf{D} as in the maintext, we obtain the following results:

TABLE V. The distances, the bond information and the symmetry restricted interactions of corresponding Fe ions between next-nearest-neighbor (001)-planes. Here n , n' and R_l correspond to $\mathbf{J}_{\tau_n, \tau_{n'} + \mathbf{R}_l}$, where R_l and τ_n represent the lattice translation vector and the position of magnetic ions in the lattice basis. Three magnetic ions are located at τ_1 (1/2, 0, 0), τ_2 (0, 1/2, 0), and τ_3 (1/2, 1/2, 0). The equivalent $\mathbf{D}_{c'i}$'s are labeled as the sub-index of j , i.e. the $\mathbf{D}_{c'i,j}$ in the table.

Distance(Å)	n	n'	R_l	J	DM
8.11	1	1	(0,0,2)	$J_{c'1}$	$\mathbf{D}_{c'1,1}(0, 0, 0)$
	2	2	(0,0,2)	$J_{c'1}$	$\mathbf{D}_{c'1,2}(0, 0, 0)$
	3	3	(0,0,2)	$J_{c'1}$	$\mathbf{D}_{c'1,3}(0, 0, 0)$
8.49	2	1	(0,1,2)	$J_{c'2}$	$\mathbf{D}_{c'2,1}(D_{c'2}^x, \sqrt{3}D_{c'2}^x, D_{c'2}^z)$
	3	2	(0,0,2)	$J_{c'2}$	$\mathbf{D}_{c'2,2}(-2D_{c'2}^x, 0, D_{c'2}^z)$
	1	3	(0,-1,2)	$J_{c'2}$	$\mathbf{D}_{c'2,3}(D_{c'2}^x, -\sqrt{3}D_{c'2}^x, D_{c'2}^z)$
	2	1	(-1,0,2)	$J_{c'2}$	$\mathbf{D}_{c'2,4}(-D_{c'2}^x, -\sqrt{3}D_{c'2}^x, D_{c'2}^z)$
	3	2	(1,0,2)	$J_{c'2}$	$\mathbf{D}_{c'2,5}(2D_{c'2}^x, 0, D_{c'2}^z)$
	1	3	(0,0,2)	$J_{c'2}$	$\mathbf{D}_{c'2,6}(-D_{c'2}^x, \sqrt{3}D_{c'2}^x, D_{c'2}^z)$
	1	2	(1,0,2)	$J_{c'2}$	$\mathbf{D}_{c'2,7}(-D_{c'2}^x, -\sqrt{3}D_{c'2}^x, -D_{c'2}^z)$
	2	3	(-1,0,2)	$J_{c'2}$	$\mathbf{D}_{c'2,8}(2D_{c'2}^x, 0, -D_{c'2}^z)$
	3	1	(0,0,2)	$J_{c'2}$	$\mathbf{D}_{c'2,9}(-D_{c'2}^x, \sqrt{3}D_{c'2}^x, -D_{c'2}^z)$
	1	2	(0,-1,2)	$J_{c'2}$	$\mathbf{D}_{c'2,10}(D_{c'2}^x, \sqrt{3}D_{c'2}^x, -D_{c'2}^z)$
	2	3	(0,0,2)	$J_{c'2}$	$\mathbf{D}_{c'2,11}(-2D_{c'2}^x, 0, -D_{c'2}^z)$
	3	1	(0,1,2)	$J_{c'2}$	$\mathbf{D}_{c'2,12}(D_{c'2}^x, -\sqrt{3}D_{c'2}^x, -D_{c'2}^z)$

$$\begin{aligned} J_{\mathbf{R}_m + \tau_p, \mathbf{R}_{m'} + \tau_{p'}} &= J_{\mathbf{R}_l + \tau_n, \mathbf{R}_{l'} + \tau_{n'}} \\ \mathbf{D}_{\mathbf{R}_m + \tau_p, \mathbf{R}_{m'} + \tau_{p'}} &= M(\alpha) \mathbf{D}_{\mathbf{R}_l + \tau_n, \mathbf{R}_{l'} + \tau_{n'}} \end{aligned} \quad (8)$$

Meanwhile, it is should be noted that the Heisenberg and DM interactions obey the following commutation relations

$$\begin{aligned} J_{\mathbf{R}_{l'} + \tau_{n'}, \mathbf{R}_l + \tau_n} &= J_{\mathbf{R}_l + \tau_n, \mathbf{R}_{l'} + \tau_{n'}} \\ \mathbf{D}_{\mathbf{R}_{l'} + \tau_{n'}, \mathbf{R}_l + \tau_n} &= -\mathbf{D}_{\mathbf{R}_l + \tau_n, \mathbf{R}_{l'} + \tau_{n'}} \end{aligned} \quad (9)$$

According to the above equations (i.e. Eq. (8) and (9)), one can obtain the symmetry restricted magnetic interactions for kagome FeGe with space group $P6/mmm$, as shown in table III, IV and V. Note that the equivalent \mathbf{D}_i 's are labeled as the sub-index of j , i.e. the $\mathbf{D}_{i,j}$ in table III, IV and V.

C. The details of double cone structure

According to the experimental works [51, 54–56], in hexagonal FeGe there is a transition from a uniaxial spin system to a double cone spin structure at $T_{canting} = 60$ K [51], which is expressed by the following equations:

$$\begin{aligned} \langle S^x \rangle &= S \sin \theta \cos \left((\pi \pm \delta) \frac{z}{c} + \varphi \right) \\ \langle S^y \rangle &= S \sin \theta \sin \left((\pi \pm \delta) \frac{z}{c} + \varphi \right) \\ \langle S^z \rangle &= S \cos \theta \cos \left(\frac{\pi z}{c} \right) \end{aligned} \quad (10)$$

where θ is the cone half angle, and c represents the lattice parameter. If $\delta = 0$ there will be a simple tilting of the spins. When δ represents the small angle, Eq. (10) gives a double cone spin structure. Following the previous works [51, 54–56], here we consider the MAE with the expression neglecting terms of order higher than four written as

$$E_{MAE} = K_2 \sin^2 \theta + K_4 \sin^4 \theta \quad (11)$$

Therefore the total energy of Eq. (5) and Eq. (11) in double cone spin structure per unit cell could be written as

$$\begin{aligned} E(\delta, \theta) &= \sum_i N_{ci} J_{ci} (-\sin^2 \theta \cos \delta - \cos^2 \theta) \\ &+ \sum_i N_{c'i} J_{c'i} (\sin^2 \theta \cos 2\delta + \cos^2 \theta) \\ &- \sum_{i,j} D_{ci,j}^z (\sin^2 \theta \sin \delta) \\ &- \sum_{i,j} D_{c'i,j}^z (\sin^2 \theta \sin 2\delta) \\ &+ N(K_2 \sin^2 \theta + K_4 \sin^4 \theta) \end{aligned} \quad (12)$$

where N_{ci} and $N_{c'i}$ are the corresponding number of neighbors of J_{ci} and $J_{c'i}$, and N represents the number of magnetic ions in one unit cell. When DM interactions are not considered, the extremum condition in total energy gives the equilibrium value of wave vector δ with following equation [51, 56]:

$$\cos \delta = \frac{\sum_i N_{ci} J_{ci}}{4 \sum_i N_{c'i} J_{c'i}} \quad (13)$$

While the cone half angle θ has the expression as

$$\sin^2 \theta = -\frac{K_2 - \frac{1}{2N} \sum_i N_{c'i} J_{c'i} \delta^4}{2K_4} \quad (14)$$

A minimum in the total energy (see Eq. (12)) will occur only if K_4 is positive, and Eq. (14) requires that $K_2 - \frac{1}{2N} \sum_i N_{c'i} J_{c'i} \delta^4$ must be negative.

When the magnetic interactions including Heisenberg and DM interactions between two nearest neighbor xy-planes, i.e. J_{ci} and \mathbf{D}_{ci} , are considered, the equilibrium value of wave vector δ is obtained by the minimum in total energy written as

$$\tan \delta = \frac{\sum_{i,j} D_{ci,j}^z}{\sum_i N_{ci} J_{ci}} \quad (15)$$

where j is the sub-index of the equivalent \mathbf{D}_{ci} 's. Meanwhile, we find the following expression for θ

$$\sin^2 \theta = -\frac{K_2 - \frac{1}{2N} \sum_{i,j} D_{ci,j}^z \delta}{2K_4} \quad (16)$$

Note that in Eq. (16), DM interactions are combined with only the first order of δ , and may have much more efficient than $J_{c'i}$ in Eq. (14) since δ is small around 0.2 [51, 53]. This implies that DM interactions may be the origin of double cone structure.

D. The symmetry analysis of CDW phases

The high-temperature phase FeGe crystallizes in space group $P6/mmm$, which has the generators $\{3_{001}^+|0\}$, $\{2_{001}|0\}$, $\{2_{110}|0\}$ and $\{-1|0\}$, where the left part represents the rotation and the right part means the lattice translation (here -1 denotes the inversion symmetry). According to the inversion symmetry, the total contribution of DM interactions to the energy of double cone magnetic structure in Eq. (12) is absent, i.e. $\sum_{i,j} D_{ci,j}^z = 0$, which is easy to see from the table IV-V. Firstly, each kagome layer is still FM in the double cone magnetic state, thus the in-plane DM interactions are ineffective. For interlayer DM interactions with an inversion center such as \mathbf{D}_{c1} , the inversion symmetry restricts it to be zero as shown in table IV. Meanwhile, for other interlayer DM interactions, the inversion symmetry combine the equivalent DM interactions in pairs. For example, as shown in table IV, the $\mathbf{D}_{c2,1}$ and $\mathbf{D}_{c2,7}$ are connected by the inversion symmetry, and have opposite values. Therefore, the summation over equivalent interlayer DM interactions are all zero due to the inversion symmetry. Note that not only inversion symmetry, but mirror symmetries such as $\{m_{001}|0\}$, $\{m_{110}|0\}$, $\{m_{100}|0\}$, $\{m_{010}|0\}$, $\{m_{1-10}|0\}$, $\{m_{120}|0\}$ and $\{m_{210}|0\}$ in space group $P6/mmm$, would also make the DM contribution to the canted magnetic ground state to be zero based on the similar analysis above. Therefore, DM interactions have no contribution to double cone magnetic structure with the symmetry of high-temperature phase.

As mentioned in the maintext, since the $2 \times 2 \times 2$ supercell structure of CDW phase (compared with the nonmagnetic pristine phase) is suggested experimentally [45, 46, 48, 49], we present the possible CDW phases of kagome FeGe with $2 \times 2 \times 2$ supercell. The $2 \times 2 \times 2$ supercell without distortion has the symmetry of space group $P6/mmm$, the non-primitive translation operations $t_x \{1|1/2,0,0\}$, $t_y \{1|0,1/2,0\}$, $t_z \{1|0,0,1/2\}$, and many symmetry operations from their combinations. As the subgroups compatible with $2 \times 2 \times 2$ supercell of pristine FeGe, the structural distortion of CDW phases would break the non-primitive translation operations t_x , t_y and t_z , and possibly break other symmetry operations as well. Since the point group associated with high-temperature phase FeGe ($P6/mmm$) is D_{6h} , we consider all CDW phases whose associated point group is D_{6h} itself or in maximal subgroups of D_{6h} (D_{2h} , D_6 , C_{6h} , C_{6v} , D_{3d} , D_{3h}). In total we find 68 different possible CDW phases, and list the corresponding relations of atomic positions in the high-temperature phase and all types of

proposed CDW phases in table VI-X. Note that the inversion symmetry and mirror symmetries in parent group $P6/mmm$ would all eliminate the contribution of DM interactions based on the symmetry analysis. Among these 68 proposed CDW phases, only four distorted structures do not have the inversion symmetry and mirror symmetries, which can lead to non-zero DM contribution to double cone spin structure and may explain this magnetic ground state. They belong to two space groups $P622$ and $P6_322$, and we list the corresponding Wyckoff positions and the coordinates of the atoms in the pristine phase and these four CDW phases in table II of the maintext.

TABLE VI. The corresponding Wyckoff positions and the coordinates of the atoms in the pristine phase and CDW phases with different symmetries. (PART I).

Pristine phase(P6/mmm)			SG191-P6/mmm(type I)			SG191-P6/mmm(type II)			SG194-P6 ₃ /mmc(type I)			SG194-P6 ₃ /mmc(type II)		
WP	Coordinates		WP	Coordinates		WP	Coordinates		WP	Coordinates		WP	Coordinates	
Ge1 1a	(0, 0, 0)		Ge1 1a	(0, 0, 0)		Ge1 2e	(0, 0, z)		Ge1 2a	(0, 0, 0)		Ge1 2b	(0, 0, 1/4)	
			Ge2 1b	(0, 0, 1/2)		Ge2 6i	(1/2, 0, z)		Ge2 6g	(1/2, 0, 0)		Ge2 6h	(x, 2x, 1/4)	
			Ge3 3f	(1/2, 0, 0)										
			Ge4 3g	(1/2, 0, 1/2)										
Ge2 2d	(1/3, 2/3, 1/2)		Ge5 4h	(1/3, 2/3, z)		Ge3 2c	(1/3, 2/3, 0)		Ge3 2c	(1/3, 2/3, 1/4)		Ge3 4f	(1/3, 2/3, z)	
			Ge6 12o	(x, 2x, z)		Ge4 2d	(1/3, 2/3, 1/2)		Ge4 2d	(1/3, 2/3, 1/4)		Ge4 12k	(x, 2x, z)	
						Ge5 6l	(x, 2x, 0)		Ge5 6h	(x, 2x, 1/4)				
						Ge6 6m	(x, 2x, 1/2)		Ge6 6h	(x, 2x, 1/4)				
Fe 3f	(1/2, 0, 0))		Fe1 6j	(x, 0, 0)		Fe1 12n	(x, 2x, z)		Fe1 12k	(x, 0, 0)		Fe1 6h	(x, 2x, 1/4)	
			Fe2 6k	(x, 0, 1/2)		Fe2 12o	(x, 0, z)		Fe2 12k	(x, 2x, z)		Fe2 6h	(x, 2x, 1/4)	
			Fe3 6l	(x, 2x, 0)								Fe3 12j	(x, y, 1/4)	
			Fe4 6m	(x, 2x, 1/2)										

Pristine phase(P6/mmm)			SG193-P6 ₃ /mcm(type I)			SG193-P6 ₃ /mcm(type II)			SG192-P6/mcc(type I)			SG192-P6/mcc(type II)		
WP	Coordinates		WP	Coordinates		WP	Coordinates		WP	Coordinates		WP	Coordinates	
Ge1 1a	(0, 0, 0)		Ge1 2b	(0, 0, 0)		Ge1 2a	(0, 0, 1/4)		Ge1 2b	(0, 0, 0)		Ge1 2b	(0, 0, 1/4)	
			Ge2 6f	(1/2, 0, 0)		Ge2 6g	(x, 0, 1/4)		Ge2 6g	(1/2, 0, 0)		Ge2 6f	(1/2, 0, 1/4)	
Ge2 2d	(1/3, 2/3, 1/2)		Ge3 4c	(1/3, 2/3, 1/4)		Ge3 4d	(1/3, 2/3, 0)		Ge3 4c	(1/3, 2/3, 1/4)		Ge3 4d	(1/3, 2/3, z)	
			Ge4 12j	(x, y, 1/4)		Ge4 12i	(x, 2x, 0)		Ge4 12k	(x, 2x, 1/4)		Ge4 12l	(x, y, 0)	
Fe 3f	(1/2, 0, 0))		Fe1 12i	(x, 0, z)		Fe1 6g	(x, 0, 1/4)		Fe1 12l	(x, y, 0)		Fe1 12j	(x, 0, 1/4)	
			Fe2 12k	(x, 2x, 0)		Fe2 6g	(x, 0, 1/4)		Fe2 12l	(x, y, 0)		Fe2 12k	(x, 2x, 1/4)	
						Fe3 12j	(x, y, 1/4)							

Pristine phase(P6/mmm)			SG190-P6 ₂ c(type I)			SG190-P6 ₂ c(type II)			SG189-P6 ₂ m(type I)			SG189-P6 ₂ m(type II)		
WP	Coordinates		WP	Coordinates		WP	Coordinates		WP	Coordinates		WP	Coordinates	
Ge1 1a	(0, 0, 0)		Ge1 2a	(0, 0, 0)		Ge1 2b	(0, 0, 1/4)		Ge1 1a	(0, 0, 0)		Ge1 2e	(0, 0, z)	
			Ge2 6g	(x, 0, 0)		Ge2 6h	(x, y, 1/4)		Ge2 1b	(0, 0, 1/2)		Ge2 6i	(x, 0, z)	
									Ge3 3f	(x, 0, 0)				
Ge2 2d	(1/3, 2/3, 1/2)		Ge3 2c	(1/3, 2/3, 1/4)		Ge3 4f	(1/3, 2/3, z)		Ge5 4h	(1/3, 2/3, z)		Ge3 2c	(1/3, 2/3, 0)	
			Ge4 2d	(1/3, 2/3, 3/4)		Ge4 12i	(x, y, z)		Ge6 12l	(x, y, z)		Ge4 2d	(1/3, 2/3, 1/2)	
			Ge5 6h	(x, y, 1/4)								Ge5 6j	(x, y, 0)	
			Ge6 6h	(x, y, 1/4)								Ge6 6k	(x, y, 1/2)	
Fe 3f	(1/2, 0, 0))		Fe1 6g	(x, 0, 0)		Fe1 6h	(x, y, 1/4)		Fe1 3f	(x, 0, 0)		Fe1 6i	(x, 0, z)	
			Fe2 6g	(x, 0, 0)		Fe2 6h	(x, y, 1/4)		Fe2 3f	(x, 0, 0)		Fe2 6i	(x, 0, z)	
			Fe3 12i	(x, y, z)		Fe3 6h	(x, y, 1/4)		Fe3 3g	(x, 0, 1/2)		Fe3 12l	(x, y, z)	
						Fe4 6h	(x, y, 1/4)		Fe4 3g	(x, 0, 1/2)				
									Fe5 6j	(x, y, 0)				
									Fe6 6k	(x, y, 1/2)				

Pristine phase(P6/mmm)			SG188-P6 ₂ c2(type I)			SG188-P6 ₂ c2(type II)			SG187-P6 ₂ m2(type I)			SG187-P6 ₂ m2(type II)		
WP	Coordinates		WP	Coordinates		WP	Coordinates		WP	Coordinates		WP	Coordinates	
Ge1 1a	(0, 0, 0)		Ge1 2a	(0, 0, 0)		Ge1 2d	(1/3, 2/3, 1/4)		Ge1 1a	(0, 0, 0)		Ge1 2h	(1/3, 2/3, z)	
			Ge2 6j	(x, 2x, 0)		Ge2 6k	(x, y, 1/4)		Ge2 1b	(0, 0, 1/2)		Ge2 6n	(x, 2x, z)	
									Ge3 3j	(x, 2x, 0)				
Ge2 2d	(1/3, 2/3, 1/2)		Ge3 2d	(2/3, 1/3, 1/4)		Ge3 2a	(0, 0, 0)		Ge5 2i	(2/3, 1/3, z)		Ge3 1a	(0, 0, 0)	
			Ge4 2f	(1/3, 2/3, 1/4)		Ge4 2e	(2/3, 1/3, 0)		Ge6 2h	(1/3, 2/3, z)		Ge4 1b	(0, 0, 1/2)	
			Ge5 6k	(x, y, 1/4)		Ge5 6j	(x, 2x, 0)		Ge7 6n	(x, 2x, z)		Ge5 1e	(2/3, 1/3, 0)	
			Ge6 6k	(x, y, 1/4)		Ge6 6j	(x, 2x, 1/2)		Ge8 6n	(x, 2x, z)		Ge6 1f	(2/3, 1/3, 1/2)	
												Ge7 3j	(x, 2x, 0)	
Fe 3f	(1/2, 0, 0)											Ge8 3j	(x, 2x, 0)	
			Fe1 6j	(x, 2x, 0)		Fe1 6k	(x, y, 1/4)		Fe1 3j	(x, 2x, 0)		Ge9 3k	(x, 2x, 1/2)	
			Fe2 6j	(x, 2x, 0)		Fe2 6k	(x, y, 1/4)		Fe2 3j	(x, 2x, 0)		Ge10 3k	(x, 2x, 1/2)	
			Fe3 12l	(x, y, z)		Fe3 6k	(x, y, 1/4)		Fe3 3k	(x, 2x, 1/2)				
						Fe4 6k	(x, y, 1/4)		Fe4 3k	(x, 2x, 1/2)				
									Fe5 6l	(x, y, 0)				
									Fe6 6m	(x, y, 1/2)				

TABLE VII. The corresponding Wyckoff positions and the coordinates of the atoms in the pristine phase and CDW phases with different symmetries. (PART II).

Pristine phase(P6/mmm)			SG186-P ₆₃ mc(type I)			SG185-P ₆₃ cm(type I)			SG184-P6cc(type I)			SG183-P6mm(type I)		
WP	Coordinates		WP	Coordinates		WP	Coordinates		WP	Coordinates		WP	Coordinates	
Ge1 1a	(0, 0, 0)		Ge1 2a	(0, 0, z)		Ge1 2a	(0, 0, z)		Ge1 2a	(0, 0, z)		Ge1 1a	(0, 0, z)	
			Ge2 6c	(x, 0, z)		Ge2 6c	(x, 2x, z)		Ge2 6c	(1/2, 0, z)		Ge2 1a	(0, 0, z)	
												Ge3 3c	(1/2, 0, z)	
Ge2 2d	(1/3, 2/3, 1/2)		Ge3 4b	(1/3, 2/3, z)		Ge3 2b	(1/3, 2/3, z)		Ge3 4b	(1/3, 2/3, z)		Ge5 2b	(1/3, 2/3, z)	
			Ge4 12d	(x, y, z)		Ge4 2b	(1/3, 2/3, z)		Ge4 12d	(x, y, z)		Ge6 2b	(1/3, 2/3, z)	
						Ge5 6c	(x, 2x, z)					Ge7 6e	(x, 2x, z)	
						Ge6 6c	(x, 2x, z)					Ge8 6e	(x, 2x, z)	
Fe 3f	(1/2, 0, 0)		Fe1 6c	(x, 0, z)		Fe1 6c	(x, 2x, z)		Fe1 12d	(x, y, z)		Fe1 6d	(x, 0, z)	
			Fe2 6c	(x, 0, z)		Fe2 6c	(x, 2x, z)		Fe2 12d	(x, y, z)		Fe2 6d	(x, 0, z)	
			Fe3 12d	(x, y, z)		Fe3 12d	(x, y, z)					Fe3 6d	(x, 2x, z)	
												Fe4 6d	(x, 2x, z)	

Pristine phase(P6/mmm)			SG182-P ₆₃ 22(type I)			SG182-P ₆₃ 22(type II)			SG177-P622(type I)			SG177-P622(type II)		
WP	Coordinates		WP	Coordinates		WP	Coordinates		WP	Coordinates		WP	Coordinates	
Ge1 1a	(0, 0, 0)		Ge1 2a	(0, 0, 0)		Ge1 2b	(0, 0, 1/4)		Ge1 1a	(0, 0, 0)		Ge1 2e	(0, 0, z)	
			Ge2 6g	(x, 0, 0)		Ge2 6h	(x, 2x, 1/4)		Ge2 1b	(0, 0, 1/2)		Ge2 6i	(1/2, 0, z)	
									Ge3 3f	(0, 1/2, 0)				
Ge2 2d	(1/3, 2/3, 1/2)		Ge3 2c	(1/3, 2/3, 1/4)		Ge3 4f	(1/3, 2/3, z)		Ge5 4h	(1/3, 2/3, z)		Ge3 2c	(1/3, 2/3, 0)	
			Ge4 2d	(1/3, 2/3, 3/4)		Ge4 12i	(x, y, z)		Ge6 12n	(x, y, z)		Ge4 2d	(1/3, 2/3, 1/2)	
			Ge5 6h	(x, 2x, 1/4)								Ge5 6l	(x, 2x, 0)	
			Ge6 6h	(x, 2x, 1/4)								Ge6 6m	(x, 2x, 1/2)	
Fe 3f	(1/2, 0, 0)		Fe1 6g	(x, 0, 0)		Fe1 6h	(x, 2x, 1/4)		Fe1 6j	(x, 0, 0)		Fe1 12n	(x, y, z)	
			Fe2 6g	(x, 0, 0)		Fe2 6h	(x, 2x, 1/4)		Fe2 6k	(x, 0, 1/2)		Fe1 12n	(x, y, z)	
			Fe3 12i	(x, y, z)		Fe3 12i	(x, y, z)		Fe3 6l	(x, 2x, 0)				
								Fe4 6m	(x, 2x, 1/2)					

Pristine phase(P6/mmm)			SG176-P ₆₃ /m(type I)			SG176-P ₆₃ /m(type II)			SG175-P6/m(type I)			SG175-P6/m(type II)		
WP	Coordinates		WP	Coordinates		WP	Coordinates		WP	Coordinates		WP	Coordinates	
Ge1 1a	(0, 0, 0)		Ge1 2b	(0, 0, 0)		Ge1 2a	(0, 0, 1/4)		Ge1 1a	(0, 0, 0)		Ge1 2e	(0, 1/2, z)	
			Ge2 6g	(1/2, 0, 0)		Ge2 6h	(x, y, 1/4)		Ge2 1b	(0, 0, 1/2)		Ge2 6i	(0, 0, z)	
									Ge3 3f	(1/2, 0, 0)				
Ge2 2d	(1/3, 2/3, 1/2)		Ge3 2c	(1/3, 2/3, 1/4)		Ge3 4f	(1/3, 2/3, z)		Ge5 4h	(1/3, 2/3, z)		Ge3 2c	(1/3, 2/3, 0)	
			Ge4 2d	(1/3, 2/3, 3/4)		Ge4 12i	(x, y, z)		Ge6 12l	(x, y, z)		Ge4 2d	(1/3, 2/3, 1/2)	
			Ge5 6h	(x, y, 1/4)								Ge5 6j	(x, y, 0)	
			Ge6 6h	(x, y, 1/4)								Ge6 6k	(x, y, 1/2)	
Fe 3f	(1/2, 0, 0)		Fe1 12i	(x, y, z)		Fe1 6h	(x, y, 1/4)		Fe1 6j	(x, y, 0)		Fe1 12l	(x, y, z)	
			Fe2 12i	(x, y, z)		Fe2 6h	(x, y, 1/4)		Fe2 6j	(x, y, 0)		Fe2 12l	(x, y, z)	
							Fe3 6h		(x, y, 1/4)	Fe3 6k		(x, y, 1/2)		
						Fe4 6h	(x, y, 1/4)		Fe4 6k	(x, y, 1/2)				

Pristine phase(P6/mmm)			SG165-P ₃ c1(type I)			SG165-P ₃ c1(type II)			SG164-P ₃ m1(type I)			SG164-P ₃ m1(type II)		
WP	Coordinates		WP	Coordinates		WP	Coordinates		WP	Coordinates		WP	Coordinates	
Ge1 1a	(0, 0, 0)		Ge1 2b	(0, 0, 0)		Ge1 2a	(0, 0, 1/4)		Ge1 1a	(0, 0, 0)		Ge1 2c	(0, 0, z)	
			Ge2 6e	(1/2, 0, 0)		Ge2 6f	(x, 0, 1/4)		Ge2 1b	(0, 0, 1/2)		Ge2 6i	(x, 2x, z)	
									Ge3 3e	(0, 1/2, 0)				
Ge2 2d	(1/3, 2/3, 1/2)		Ge3 4d	(1/3, 2/3, z)		Ge3 4d	(1/3, 2/3, z)		Ge5 2d	(1/3, 2/3, z)		Ge3 2d	(1/3, 2/3, z)	
			Ge4 12g	(x, y, z)		Ge4 12g	(x, y, z)		Ge6 2d	(1/3, 2/3, z)		Ge4 2d	(1/3, 2/3, z)	
									Ge7 6i	(x, 2x, z)		Ge5 6i	(x, 2x, z)	
									Ge8 6i	(x, 2x, z)		Ge6 6i	(x, 2x, z)	
Fe 3f	(1/2, 0, 0)		Fe1 12g	(x, y, z)		Fe1 6f	(x, 0, 1/4)		Fe1 6i	(x, 2x, z)		Fe1 6i	(x, 2x, z)	
			Fe2 12g	(x, y, z)		Fe2 6f	(x, 0, 1/4)		Fe2 6i	(x, 2x, z)		Fe2 6i	(x, 2x, z)	
						Fe3 12g	(x, y, z)		Fe3 12j	(x, y, z)		Fe3 12j	(x, y, z)	

TABLE VIII. The corresponding Wyckoff positions and the coordinates of the atoms in the pristine phase and CDW phases with different symmetries. (PART III).

Pristine phase(P6/mmm)			SG163-P $\bar{3}$ 1c(type I)			SG163-P $\bar{3}$ 1c(type II)			SG162-P $\bar{3}$ 1m(type I)			SG162-P $\bar{3}$ 1m(type II)		
WP	Coordinates		WP	Coordinates		WP	Coordinates		WP	Coordinates		WP	Coordinates	
Ge1 1a	(0, 0, 0)		Ge1 2b	(0, 0, 0)		Ge1 2a	(0, 0, 1/4)		Ge1 1a	(0, 0, 0)		Ge1 2e	(0, 0, z)	
			Ge2 6g	(0, 1/2, 0)		Ge2 6h	(x, 2x, 1/4)		Ge2 1b	(0, 0, 1/2)		Ge2 6k	(x, 0, z)	
									Ge3 3f	(1/2, 0, 0)				
Ge2 2d	(1/3, 2/3, 1/2)		Ge3 2c	(1/3, 2/3, 1/4)		Ge3 4f	(1/3, 2/3, z)		Ge5 4h	(1/3, 2/3, z)		Ge3 2c	(1/3, 2/3, 0)	
			Ge4 2d	(1/3, 2/3, 3/4)		Ge4 12i	(x, y, z)		Ge6 12l	(x, y, z)		Ge4 2d	(1/3, 2/3, 1/2)	
			Ge5 6h	(x, 2x, 1/4)								Ge5 6i	(x, 2x, 0)	
			Ge6 6h	(x, 2x, 1/4)								Ge6 6j	(x, 2x, 1/2)	
Fe 3f	(1/2, 0, 0))		Fe1 12i	(x, y, z)		Fe1 6h	(x, 2x, 1/4)		Fe1 6i	(x, 2x, 0)		Fe1 6k	(x, 0, z)	
			Fe2 12i	(x, y, z)		Fe2 6h	(x, 2x, 1/4)		Fe2 6j	(x, 2x, 1/2)		Fe2 6k	(x, 0, z)	
						Fe3 12i	(x, y, z)		Fe3 6k	(x, 0, z)		Fe3 12i	(x, y, z)	
									Fe4 6k	(x, 0, z)				

Pristine phase(P6/mmm)			SG68-Ccce(type I)			SG68-Ccce(type II)			SG68-Ccce(type III)			SG68-Ccce(type IV)		
WP	Coordinates		WP	Coordinates		WP	Coordinates		WP	Coordinates		WP	Coordinates	
Ge1 1a	(0, 0, 0)		Ge1 8c	(1/4, 1/4, 0)		Ge1 8e	(x, 1/4, 1/4)		Ge1 8g	(0, 1/4, z)		Ge1 4a	(0, 1/4, 1/4)	
			Ge2 8d	(0, 0, 0)		Ge2 8f	(0, y, 1/4)		Ge2 8h	(1/4, 0, z)		Ge2 4b	(0, 1/4, 3/4)	
Ge2 2d	(1/3, 2/3, 1/2)											Ge3 8h	(1/4, 0, z)	
			Ge3 8f	(0, y, 1/4)		Ge3 16i	(x, y, z)		Ge3 8f	(0, y, 1/4)		Ge3 16i	(x, y, z)	
			Ge4 8f	(0, y, 1/4)		Ge4 16i	(x, y, z)		Ge4 8f	(0, y, 1/4)		Ge4 16i	(x, y, z)	
Fe 3f	(1/2, 0, 0))		Ge5 16i	(x, y, z)					Ge5 16i	(x, y, z)				
			Fe1 8g	(0, 1/4, z)		Fe1 4a	(0, 1/4, 1/4)		Fe1 8c	(1/4, 1/4, 0)		Fe1 8e	(x, 1/4, 1/4)	
			Fe2 8h	(1/4, 0, z)		Fe2 4b	(0, 1/4, 3/4)		Fe2 8d	(0, 0, 1/2)		Fe2 8f	(0, y, 1/4)	
			Fe3 16i	(x, y, z)		Fe3 8h	(1/4, 0, z)		Fe3 16i	(x, y, z)		Fe3 16i	(x, y, z)	
			Fe4 16i	(x, y, z)		Fe4 16i	(x, y, z)		Fe4 16i	(x, y, z)		Fe4 16i	(x, y, z)	
						Fe5 16i	(x, y, z)							

Pristine phase(P6/mmm)			SG67-Cmme(type I)			SG67-Cmme(type II)			SG67-Cmme(type III)			SG67-Cmme(type IV)		
WP	Coordinates		WP	Coordinates		WP	Coordinates		WP	Coordinates		WP	Coordinates	
Ge1 1a	(0, 0, 0)		Ge1 4c	(0, 0, 0)		Ge1 4a	(1/4, 0, 0)		Ge1 4g	(0, 1/4, z)		Ge1 8n	(x, 1/4, z)	
			Ge2 4d	(0, 0, 1/2)		Ge2 4b	(1/4, 0, 1/2)		Ge2 4g	(0, 1/4, z)		Ge2 8m	(0, y, z)	
			Ge3 4e	(1/4, 1/4, 0)		Ge3 4g	(0, 1/4, z)		Ge3 8l	(1/4, 0, z)				
			Ge4 4f	(1/4, 1/4, 1/2)		Ge4 4g	(0, 1/4, z)							
Ge2 2d	(1/3, 2/3, 1/2)		Ge5 8m	(0, y, z)		Ge5 8m	(0, y, z)		Ge4 8j	(1/4, y, 0)		Ge3 8j	(1/4, y, 0)	
			Ge6 8m	(0, y, z)		Ge6 8m	(0, y, z)		Ge5 8k	(1/4, y, 1/2)		Ge4 8k	(1/4, y, 1/2)	
			Ge7 16o	(x, y, z)		Ge7 16o	(x, y, z)		Ge6 8m	(0, y, z)		Ge5 8m	(0, y, z)	
									Ge7 8m	(0, y, z)		Ge6 8m	(0, y, z)	
Fe 3f	(1/2, 0, 0))		Fe1 4a	(1/4, 0, 0)		Fe1 4c	(0, 0, 0)		Fe1 8n	(x, 1/4, z)		Fe1 4g	(0, 1/4, z)	
			Fe2 4b	(1/4, 0, 1/2)		Fe2 4d	(0, 0, 1/2)		Fe2 8m	(0, y, z)		Fe2 4g	(0, 1/4, z)	
			Fe3 4g	(0, 1/4, z)		Fe3 4e	(1/4, 1/4, 0)		Fe3 16o	(x, y, z)		Fe3 8l	(1/4, 0, z)	
			Fe4 4g	(0, 1/4, z)		Fe4 4f	(1/4, 1/4, 1/2)		Fe4 16o	(x, y, z)		Fe4 16o	(x, y, z)	
			Fe5 16o	(x, y, z)		Fe5 16o	(x, y, z)					Fe5 16o	(x, y, z)	
			Fe6 16o	(x, y, z)		Fe6 16o	(x, y, z)							

Pristine phase(P6/mmm)			SG66-Cccm(type I)			SG66-Cccm(type II)			SG66-Cccm(type III)			SG66-Cccm(type IV)		
WP	Coordinates		WP	Coordinates		WP	Coordinates		WP	Coordinates		WP	Coordinates	
Ge1 1a	(0, 0, 0)		Ge1 4c	(0, 0, 0)		Ge1 4a	(0, 0, 1/4)		Ge1 8l	(x, y, 0)		Ge1 8g	(x, 0, 1/4)	
			Ge2 4d	(0, 0, 1/2)		Ge2 4b	(0, 1/2, 1/4)		Ge2 8l	(x, y, 0)		Ge2 8h	(0, y, 1/4)	
			Ge3 4e	(1/4, 1/4, 0)		Ge3 8k	(1/4, 1/4, 1/4)							
			Ge4 4f	(1/4, 1/4, 1/2)										
Ge2 2d	(1/3, 2/3, 1/2)		Ge5 8h	(0, y, 1/4)		Ge4 8l	(x, y, 0)		Ge3 8h	(0, y, 1/4)		Ge3 8l	(x, y, 0)	
			Ge6 8h	(0, y, 1/4)		Ge5 8l	(x, y, 0)		Ge4 8h	(0, y, 1/4)		Ge4 8l	(x, y, 0)	
			Ge7 16m	(x, y, z)		Ge6 8l	(x, y, 0)		Ge5 16m	(x, y, z)		Ge5 8l	(x, y, 0)	
						Ge7 8l	(x, y, 0)					Ge6 8l	(x, y, 0)	
Fe 3f	(1/2, 0, 0))		Fe1 8l	(x, y, 0)		Fe1 8g	(x, 0, 1/4)		Fe1 4c	(0, 0, 0)		Fe1 4a	(0, 0, 1/4)	
			Fe2 8l	(x, y, 0)		Fe2 8h	(0, y, 1/4)		Fe2 4d	(0, 0, 1/2)		Fe2 4b	(0, 1/2, 1/4)	
			Fe3 8l	(x, y, 0)		Fe3 16m	(x, y, z)		Fe3 4e	(1/4, 1/4, 0)		Fe3 8k	(1/4, 1/4, 1/4)	
			Fe4 8l	(x, y, 0)		Fe4 16m	(x, y, z)		Fe4 4f	(1/4, 1/4, 1/2)		Fe4 16m	(x, y, z)	
			Fe5 8l	(x, y, 0)					Fe5 8l	(x, y, 0)		Fe5 16m	(x, y, z)	
			Fe6 8l	(x, y, 0)					Fe6 8l	(x, y, 0)				
									Fe7 8l	(x, y, 0)				
									Fe8 8l	(x, y, 0)				

TABLE IX. The corresponding Wyckoff positions and the coordinates of the atoms in the pristine phase and CDW phases with different symmetries. (PART IV).

Pristine phase(P6/mmm)		SG65-Cmmm(type I)		SG65-Cmmm(case2)		SG65-Cmmm(type III)		SG65-Cmmm(type IV)	
WP	Coordinates	WP	Coordinates	WP	Coordinates	WP	Coordinates	WP	Coordinates
Ge1 1a	(0, 0, 0)	Ge1 2a	(0, 0, 0)	Ge1 4i	(0, y, 0)	Ge1 4k	(0, 0, z)	Ge1 8o	(x, 0, z)
		Ge2 2b	(0, 1/2, 0)	Ge2 4j	(0, y, 1/2)	Ge2 4l	(0, 1/2, z)	Ge2 8n	(0, y, z)
		Ge3 2c	(0, 1/2, 1/2)	Ge3 4g	(x, 0, 0)	Ge3 8m	(1/4, 1/4, z)		
		Ge4 2d	(0, 0, 1/2)	Ge4 4h	(x, 0, 1/2)				
		Ge5 4e	(1/4, 1/4, 0)						
		Ge6 4f	(1/4, 1/4, 1/2)						
Ge2 2d	(1/3, 2/3, 1/2)	Ge7 8n	(0, y, z)	Ge5 8n	(0, y, z)	Ge4 4i	(0, y, 0)	Ge3 4i	(0, y, 0)
		Ge8 8n	(0, y, z)	Ge6 8n	(0, y, z)	Ge5 4i	(0, y, 0)	Ge4 4i	(0, y, 0)
		Ge9 16r	(x, y, z)	Ge7 16r	(x, y, z)	Ge6 4j	(0, y, 1/2)	Ge5 4j	(0, y, 1/2)
						Ge7 4j	(0, y, 1/2)	Ge6 4j	(0, y, 1/2)
						Ge8 8p	(x, y, 0)	Ge7 8p	(x, y, 0)
						Ge9 8q	(x, y, 1/2)	Ge8 8q	(x, y, 1/2)
Fe 3f	(1/2, 0, 0)	Fe1 4g	(x, 0, 0)	Fe1 2a	(0, 0, 0)	Fe1 8o	(x, 0, z)	Fe1 4k	(0, 0, z)
		Fe2 4h	(x, 0, 1/2)	Fe2 2b	(0, 1/2, 0)	Fe2 8n	(0, y, z)	Fe2 4l	(0, 1/2, z)
		Fe3 4i	(0, y, 0)	Fe3 2c	(0, 1/2, 1/2)	Fe3 16r	(x, y, z)	Fe3 8m	(1/4, 1/4, z)
		Fe4 4j	(0, y, 1/2)	Fe4 2d	(0, 0, 1/2)	Fe4 16r	(x, y, z)	Fe4 16r	(x, y, z)
		Fe5 8p	(x, y, 0)	Fe5 4e	(1/4, 1/4, 0)			Fe5 16r	(x, y, z)
		Fe6 8p	(x, y, 0)	Fe6 4f	(1/4, 1/4, 1/2)				
		Fe7 8q	(x, y, 1/2)	Fe7 8p	(x, y, 0)				
		Fe8 8q	(x, y, 1/2)	Fe8 8p	(x, y, 0)				
				Fe9 8q	(x, y, 1/2)				
				Fe10 8q	(x, y, 1/2)				

Pristine phase(P6/mmm)		SG64-Cmce(type I)		SG64-Cmce(type II)		SG64-Cmce(type III)		SG64-Cmce(type IV)	
WP	Coordinates	WP	Coordinates	WP	Coordinates	WP	Coordinates	WP	Coordinates
Ge1 1a	(0, 0, 0)	Ge1 4a	(0, 0, 0)	Ge1 4a	(0, 0, 0)	Ge1 8e	(1/4, y, 1/4)	Ge1 8e	(1/4, y, 1/4)
		Ge2 4b	(0, 0, 1/2)	Ge2 4b	(0, 0, 1/2)	Ge2 8f	(0, y, z)	Ge2 8f	(0, y, z)
		Ge3 8c	(1/4, 1/4, 0)	Ge3 8c	(1/4, 1/4, 0)				
Ge2 2d	(1/3, 2/3, 1/2)	Ge4 16g	(x, y, z)	Ge4 8e	(1/4, y, 1/4)	Ge3 8d	(x, 0, 0)	Ge3 8f	(0, y, z)
		Ge5 16g	(x, y, z)	Ge5 8e	(1/4, y, 1/4)	Ge4 8d	(x, 0, 0)	Ge4 8f	(0, y, z)
				Ge6 8f	(0, y, z)	Ge5 16g	(x, y, z)	Ge5 16g	(x, y, z)
				Ge7 8f	(0, y, z)				
Fe 3f	(1/2, 0, 0))	Fe1 8d	(x, 0, 0)	Fe1 8e	(1/4, y, 1/4)	Fe1 8e	(1/4, y, 1/4)	Fe1 8e	(1/4, y, 1/4)
		Fe2 8f	(0, y, z)	Fe2 8f	(0, y, z)	Fe2 8f	(0, y, z)	Fe2 8f	(0, y, z)
		Fe3 16g	(x, y, z)	Fe3 16g	(x, y, z)	Fe3 16g	(x, y, z)	Fe3 16g	(x, y, z)
		Fe4 16g	(x, y, z)	Fe4 16g	(x, y, z)	Fe4 16g	(x, y, z)	Fe4 16g	(x, y, z)

Pristine phase(P6/mmm)		SG64-Cmce(type V)		SG64-Cmce(type VI)		SG64-Cmce(type VII)		SG64-Cmce(type VIII)	
WP	Coordinates	WP	Coordinates	WP	Coordinates	WP	Coordinates	WP	Coordinates
Ge1 1a	(0, 0, 0)	Ge1 8e	(1/4, y, 1/4)	Ge1 8e	(1/4, y, 1/4)	Ge1 8d	(x, 0, 0)	Ge1 8d	(x, 0, 0)
		Ge2 8f	(0, y, z)	Ge2 8f	(0, y, z)	Ge2 8f	(0, y, z)	Ge2 8f	(0, y, z)
Ge2 2d	(1/3, 2/3, 1/2)	Ge3 8f	(0, y, z)	Ge3 8d	(x, 0, 0)	Ge3 16g	(x, y, z)	Ge4 8e	(1/4, y, 1/4)
		Ge4 8f	(0, y, z)	Ge4 8d	(x, 0, 0)	Ge4 16g	(x, y, z)	Ge5 8e	(1/4, y, 1/4)
		Ge5 16g	(x, y, z)	Ge5 16g	(x, y, z)			Ge6 8f	(0, y, z)
Fe 3f	(1/2, 0, 0))							Ge7 8f	(0, y, z)
		Fe1 8e	(1/4, y, 1/4)	Fe1 8e	(1/4, y, 1/4)	Fe1 4a	(0, 0, 0)	Fe1 4a	(0, 0, 0)
		Fe2 8f	(0, y, z)	Fe2 8f	(0, y, z)	Fe2 4b	(0, 0, 1/2)	Fe2 4b	(0, 0, 1/2)
		Fe3 16g	(x, y, z)	Fe3 16g	(x, y, z)	Fe3 8c	(1/4, 1/4, 0)	Fe3 8c	(1/4, 1/4, 0)
		Fe4 16g	(x, y, z)	Fe4 16g	(x, y, z)	Fe4 16g	(x, y, z)	Fe4 16g	(x, y, z)
						Fe5 16g	(x, y, z)	Fe5 16g	(x, y, z)

TABLE X. The corresponding Wyckoff positions and the coordinates of the atoms in the pristine phase and CDW phases with different symmetries. (PART V).

Pristine phase(P6/mmm)			SG63-Cmcm(type I)			SG63-Cmcm(type II)			SG63-Cmcm(type III)			SG63-Cmcm(type IV)		
WP	Coordinates		WP	Coordinates		WP	Coordinates		WP	Coordinates		WP	Coordinates	
Ge1 1a	(0, 0, 0)		Ge1 4a	(0, 0, 0)		Ge1 4a	(0, 0, 0)		Ge1 4c	(0, y, 1/4)		Ge1 4c	(0, y, 1/4)	
			Ge2 4b	(0, 1/2, 0)		Ge2 4b	(0, 1/2, 0)		Ge2 4c	(0, y, 1/4)		Ge2 4c	(0, y, 1/4)	
			Ge3 8d	(1/4, 1/4, 0)		Ge3 8d	(1/4, 1/4, 0)		Ge3 8g	(x, y, 1/4)		Ge3 8g	(x, y, 1/4)	
Ge2 2d	(1/3, 2/3, 1/2)		Ge4 8g	(x, y, 1/4)		Ge4 4c	(0, y, 1/4)		Ge4 8e	(x, 0, 0)		Ge4 8e	(x, 0, 0)	
			Ge5 8g	(x, y, 1/4)		Ge5 4c	(0, y, 1/4)		Ge5 8e	(x, 0, 0)		Ge5 8e	(x, 0, 0)	
			Ge6 8g	(x, y, 1/4)		Ge6 4c	(0, y, 1/4)		Ge6 16h	(x, y, z)		Ge6 16h	(x, y, z)	
			Ge7 8g	(x, y, 1/4)		Ge7 4c	(0, y, 1/4)							
						Ge8 8g	(x, y, 1/4)							
						Ge9 8g	(x, y, 1/4)							
Fe 3f	(1/2, 0, 0))		Fe1 8e	(x, 0, 0)		Fe1 8e	(x, 0, 0)		Fe1 4c	(0, y, 1/4)		Fe1 4c	(0, y, 1/4)	
			Fe2 8f	(0, y, z)		Fe2 8f	(0, y, z)		Fe2 4c	(0, y, 1/4)		Fe2 4c	(0, y, 1/4)	
			Fe3 16h	(x, y, z)		Fe3 16h	(x, y, z)		Fe3 8g	(x, y, 1/4)		Fe3 8g	(x, y, 1/4)	
			Fe4 16h	(x, y, z)		Fe4 16h	(x, y, z)		Fe4 8g	(x, y, 1/4)		Fe4 8g	(x, y, 1/4)	
									Fe5 8g	(x, y, 1/4)		Fe5 8g	(x, y, 1/4)	
									Fe6 8g	(x, y, 1/4)		Fe6 8g	(x, y, 1/4)	
									Fe7 8g	(x, y, 1/4)		Fe7 8g	(x, y, 1/4)	

Pristine phase(P6/mmm)			SG63-Cmcm(type V)			SG63-Cmcm(type VI)			SG63-Cmcm(type VII)			SG63-Cmcm(type VIII)		
WP	Coordinates		WP	Coordinates		WP	Coordinates		WP	Coordinates		WP	Coordinates	
Ge1 1a	(0, 0, 0)		Ge1 4c	(0, y, 1/4)		Ge1 4c	(0, y, 1/4)		Ge1 8e	(x, 0, 0)		Ge1 8e	(x, 0, 0)	
			Ge2 4c	(0, y, 1/4)		Ge2 4c	(0, y, 1/4)		Ge2 8f	(0, y, z)		Ge2 8f	(0, y, z)	
			Ge3 8g	(x, y, 1/4)		Ge3 8g	(x, y, 1/4)							
Ge2 2d	(1/3, 2/3, 1/2)		Ge4 8f	(0, y, z)		Ge4 8f	(0, y, z)		Ge3 8g	(x, y, 1/4)		Ge4 4c	(0, y, 1/4)	
			Ge5 8f	(0, y, z)		Ge5 8f	(0, y, z)		Ge4 8g	(x, y, 1/4)		Ge5 4c	(0, y, 1/4)	
			Ge6 16h	(x, y, z)		Ge6 16h	(x, y, z)		Ge5 8g	(x, y, 1/4)		Ge6 4c	(0, y, 1/4)	
									Ge6 8g	(x, y, 1/4)		Ge7 4c	(0, y, 1/4)	
Fe 3f	(1/2, 0, 0))											Ge8 8g	(x, y, 1/4)	
			Fe1 4c	(0, y, 1/4)		Fe1 4c	(0, y, 1/4)		Fe1 4a	(0, 0, 0)		Fe1 4a	(0, 0, 0)	
			Fe2 4c	(0, y, 1/4)		Fe2 4c	(0, y, 1/4)		Fe2 4b	(0, 1/2, 0)		Fe2 4b	(0, 1/2, 0)	
			Fe3 8g	(x, y, 1/4)		Fe3 8g	(x, y, 1/4)		Fe3 8d	(1/4, 1/4, 0)		Fe3 8d	(1/4, 1/4, 0)	
			Fe4 8g	(x, y, 1/4)		Fe4 8g	(x, y, 1/4)		Fe4 16h	(x, y, z)		Fe4 16h	(x, y, z)	
			Fe5 8g	(x, y, 1/4)		Fe5 8g	(x, y, 1/4)		Fe5 16h	(x, y, z)		Fe5 16h	(x, y, z)	
			Fe6 8g	(x, y, 1/4)		Fe6 8g	(x, y, 1/4)							
			Fe7 8g	(x, y, 1/4)		Fe7 8g	(x, y, 1/4)							

-
- [1] I. Syôzi, “Statistics of kagomé lattice,” *Progress of Theoretical Physics* **6**, 306 (1951).
- [2] A. Mielke, “Ferromagnetic ground states for the Hubbard model on line graphs,” *Journal of Physics A: Mathematical and General* **24**, L73 (1991).
- [3] A. Tanaka and H. Ueda, “Stability of ferromagnetism in the Hubbard model on the Kagome lattice,” *Physical review letters* **90**, 067204 (2003).
- [4] M. L. Kiesel, C. Platt, and R. Thomale, “Unconventional Fermi surface instabilities in the kagome Hubbard model,” *Physical review letters* **110**, 126405 (2013).
- [5] T. Park, M. Ye, and L. Balents, “Electronic instabilities of kagome metals: saddle points and Landau theory,” *Physical Review B* **104**, 035142 (2021).
- [6] M. Kang, L. Ye, S. Fang, J.-S. You, A. Levitan, M. Han, J. I. Facio, C. Jozwiak, A. Bostwick, E. Rotenberg, M. K. Chan, R. D. McDonald, D. Graf, K. Kaznatcheev, E. Vescovo, D. C. Bell, E. Kaxiras, J. van den Brink, M. Richter, M. Prasad Ghimire, J. G. Checkelsky, and R. Comin, “Dirac fermions and flat bands in the ideal kagome metal FeSn,” *Nature materials* **19**, 163 (2020).
- [7] Y. Xie, L. Chen, T. Chen, Q. Wang, Q. Yin, J. R. Stewart, M. B. Stone, L. L. Daemen, E. Feng, H. Cao, H. Lei, Z. Yin, A. H. MacDonald, and P. Dai, “Spin excitations in metallic kagome lattice FeSn and CoSn,” *Communications Physics* **4**, 1 (2021).
- [8] B. C. Sales, J. Yan, W. R. Meier, A. D. Christianson, S. Okamoto, and M. A. McGuire, “Electronic, magnetic, and thermodynamic properties of the kagome layer compound FeSn,” *Physical Review Materials* **3**, 114203 (2019).
- [9] S.-H. Do, K. Kaneko, R. Kajimoto, K. Kamazawa, M. B. Stone, J. Y. Y. Lin, S. Itoh, T. Masuda, G. D. Samolyuk, E. Dagotto, W. R. Meier, B. C. Sales, H. Miao, and A. D. Christianson, “Damped Dirac magnon in the metallic kagome antiferromagnet FeSn,” *Physical Review B* **105**, L180403 (2022).
- [10] Y.-F. Zhang, X.-S. Ni, T. Datta, M. Wang, D.-X. Yao, and K. Cao, “Ab initio study on spin fluctuations of itinerant kagome magnet FeSn,” *arXiv preprint arXiv:2209.00187* (2022).
- [11] L. Ye, M. Kang, J. Liu, F. von Cube, C. R. Wicker, T. Suzuki, C. Jozwiak, A. Bostwick, E. Rotenberg, D. C. Bell, L. Fu, R. Comin, and J. G. Checkelsky, “Massive dirac fermions in a ferromagnetic kagome metal,” *Nature* **555**, 638 (2018).
- [12] Z. Lin, J.-H. Choi, Q. Zhang, W. Qin, S. Yi, P. Wang, L. Li, Y. Wang, H. Zhang, Z. Sun, L. Wei, S. Zhang, T. Guo, Q. Lu, J.-H. Cho, C. Zeng, and Z. Zhang, “Flatbands and emergent ferromagnetic ordering in Fe_3Sn_2 kagome lattices,” *Physical review letters* **121**, 096401 (2018).
- [13] N. Morali, R. Batabyal, P. K. Nag, E. Liu, Q. Xu, Y. Sun, B. Yan, C. Felser, N. Avraham, and H. Beidenkopf, “Fermi-arc diversity on surface terminations of the magnetic Weyl semimetal $\text{Co}_3\text{Sn}_2\text{S}_2$,” *Science* **365**, 1286 (2019).
- [14] D. F. Liu, A. J. Liang, E. K. Liu, Q. N. Xu, Y. W. Li, C. Chen, D. Pei, W. J. Shi, S. K. Mo, P. Dudin, T. Kim, C. Cacho, G. Li, Y. Sun, L. X. Yang, Z. K. Liu, S. S. P. Parkin, C. Felser, and Y. L. Chen, “Magnetic Weyl semimetal phase in a Kagomé crystal,” *Science* **365**, 1282 (2019).
- [15] K. Kuroda, T. Tomita, M.-T. Suzuki, C. Bareille, A. A. Nugroho, P. Goswami, M. Ochi, M. Ikhlas, M. Nakayama, S. Akebi, R. Noguchi, R. Ishii, N. Inami, K. Ono, H. Kumigashira, A. Varykhalov, T. Muro, T. Koretsune, R. Arita, S. Shin, T. Kondo, and S. Nakatsuji, “Evidence for magnetic Weyl fermions in a correlated metal,” *Nature materials* **16**, 1090 (2017).
- [16] J.-X. Yin, S. S. Zhang, G. Chang, Q. Wang, S. S. Tsirkin, Z. Guguchia, B. Lian, H. Zhou, K. Jiang, I. Belopolski, N. Shumiya, D. Multer, M. Litskevich, T. A. Cochran, H. Lin, Z. Wang, T. Neupert, S. Jia, H. Lei, and M. Z. Hasan, “Negative flat band magnetism in a spin-orbit-coupled correlated kagome magnet,” *Nature Physics* **15**, 443 (2019).
- [17] J.-X. Yin, W. Ma, T. A. Cochran, X. Xu, S. S. Zhang, H.-J. Tien, N. Shumiya, G. Cheng, K. Jiang, B. Lian, Z. Song, G. Chang, I. Belopolski, D. Multer, M. Litskevich, Z.-J. Cheng, X. P. Yang, B. Swidler, H. Zhou, H. Lin, T. Neupert, Z. Wang, N. Yao, T.-R. Chang, S. Jia, and M. Zahid Hasan, “Quantum-limit Chern topological magnetism in TbMn_6Sn_6 ,” *Nature* **583**, 533 (2020).
- [18] M. Li, Q. Wang, G. Wang, Z. Yuan, W. Song, R. Lou, Z. Liu, Y. Huang, Z. Liu, H. Lei, Z. Yin, and S. Wang, “Dirac cone, flat band and saddle point in kagome magnet YMn_6Sn_6 ,” *Nature communications* **12**, 1 (2021).
- [19] B. R. Ortiz, L. C. Gomes, J. R. Morey, M. Winiarski, M. Bordelon, J. S. Mangum, I. W. Oswald, J. A. Rodriguez-Rivera, J. R. Neilson, S. D. Wilson, *et al.*, “New kagome prototype materials: discovery of KV_3Sb_5 , RbV_3Sb_5 , and CsV_3Sb_5 ,” *Physical Review Materials* **3**, 094407 (2019).
- [20] H. Zhao, H. Li, B. R. Ortiz, S. M. Teicher, T. Park, M. Ye, Z. Wang, L. Balents, S. D. Wilson, and I. Zeljkovic, “Cascade of correlated electron states in the kagome superconductor CsV_3Sb_5 ,” *Nature* **599**, 216 (2021).
- [21] H. Chen, H. Yang, B. Hu, Z. Zhao, J. Yuan, Y. Xing, G. Qian, Z. Huang, G. Li, Y. Ye, S. Ma, S. Ni, H. Zhang, Q. Yin, C. Gong, Z. Tu, H. Lei, H. Tan, S. Zhou, C. Shen, X. Dong, B. Yan, Z. Wang, and H.-J. Gao, “Roton pair density wave in a strong-coupling kagome superconductor,” *Nature* **599**, 222 (2021).
- [22] B. R. Ortiz, S. M. L. Teicher, Y. Hu, J. L. Zuo, P. M. Sarte, E. C. Schueller, A. M. M. Abeykoon, M. J. Krogstad, S. Rosenkranz, R. Osborn, R. Seshadri, L. Balents, J. He, and S. D. Wilson, “ CsV_3Sb_5 : A z_2 topological kagome metal with a superconducting ground state,” *Physical Review Letters* **125**, 247002 (2020).
- [23] Y.-X. Jiang, J.-X. Yin, M. M. Denner, N. Shumiya, B. R. Ortiz, G. Xu, Z. Guguchia, J. He, M. S. Hossain, X. Liu, J. Ruff, L. Kautzsch, S. S. Zhang, G. Chang, I. Belopolski, Q. Zhang, T. A. Cochran, D. Multer, M. Litskevich, Z.-J. Cheng, X. P. Yang, Z. Wang, R. Thomale, T. Neupert, S. D. Wilson, and M. Z. Hasan, “Unconventional chiral charge order in kagome superconductor KV_3Sb_5 ,” *Nature Materials* **20**, 1353 (2021).
- [24] C. Mielke, D. Das, J.-X. Yin, H. Liu, R. Gupta, Y.-X. Jiang, M. Medarde, X. Wu, H. C. Lei, J. Chang,

- P. Dai, Q. Si, H. Miao, R. Thomale, T. Neupert, Y. Shi, R. Khasanov, M. Z. Hasan, H. Luetkens, and Z. Guguchia, “Time-reversal symmetry-breaking charge order in a kagome superconductor,” *Nature* **602**, 245 (2022).
- [25] M. M. Denner, R. Thomale, and T. Neupert, “Analysis of Charge Order in the Kagome Metal AV_3Sb_5 ($A = K, Rb, Cs$),” *Physical Review Letters* **127**, 217601 (2021).
- [26] Y.-P. Lin and R. M. Nandkishore, “Complex charge density waves at Van Hove singularity on hexagonal lattices: Haldane-model phase diagram and potential realization in the kagome metals AV_3Sb_5 ($A = K, Rb, Cs$),” *Physical Review B* **104**, 045122 (2021).
- [27] L. Nie, K. Sun, W. Ma, D. Song, L. Zheng, Z. Liang, P. Wu, F. Yu, J. Li, M. Shan, D. Zhao, S. Li, B. Kang, Z. Wu, Y. Zhou, K. Liu, Z. Xiang, J. Ying, Z. Wang, T. Wu, and X. Chen, “Charge-density-wave-driven electronic nematicity in a kagome superconductor,” *Nature* **604**, 59 (2022).
- [28] H. Li, T. T. Zhang, T. Yilmaz, Y. Y. Pai, C. E. Marvinney, A. Said, Q. W. Yin, C. S. Gong, Z. J. Tu, E. Vescovo, C. S. Nelson, R. G. Moore, S. Murakami, H. C. Lei, H. N. Lee, B. J. Lawrie, and H. Miao, “Observation of Unconventional Charge Density Wave without Acoustic Phonon Anomaly in Kagome Superconductors AV_3Sb_5 ($A = Rb, Cs$),” *Physical Review X* **11**, 031050 (2021).
- [29] T. Neupert, M. M. Denner, J.-X. Yin, R. Thomale, and M. Z. Hasan, “Charge order and superconductivity in kagome materials,” *Nature Physics* **18**, 137 (2022).
- [30] F. Yu, D. Ma, W. Zhuo, S. Liu, X. Wen, B. Lei, J. Ying, and X. Chen, “Unusual competition of superconductivity and charge-density-wave state in a compressed topological kagome metal,” *Nature communications* **12**, 1 (2021).
- [31] Y. Xiang, Q. Li, Y. Li, W. Xie, H. Yang, Z. Wang, Y. Yao, and H.-H. Wen, “Twofold symmetry of c -axis resistivity in topological kagome superconductor CsV_3Sb_5 with in-plane rotating magnetic field,” *Nature communications* **12**, 1 (2021).
- [32] J. Ge, P. Wang, Y. Xing, Q. Yin, H. Lei, Z. Wang, and J. Wang, “Discovery of charge-4e and charge-6e superconductivity in kagome superconductor csv_3sb_5 ,” *arXiv preprint arXiv:2201.10352* (2022).
- [33] L. Zheng, Z. Wu, Y. Yang, L. Nie, M. Shan, K. Sun, D. Song, F. Yu, J. Li, D. Zhao, S. Li, B. Kang, Y. Zhou, K. Liu, Z. Xiang, J. Ying, Z. Wang, T. Wu, and X. Chen, “Emergent charge order in pressurized kagome superconductor CsV_3Sb_5 ,” *Nature* **611**, 682 (2022).
- [34] X. Feng, K. Jiang, Z. Wang, and J. Hu, “Chiral flux phase in the Kagome superconductor AV_3Sb_5 ,” *Science bulletin* **66**, 1384 (2021).
- [35] K. Jiang, T. Wu, J.-X. Yin, Z. Wang, M. Z. Hasan, S. D. Wilson, X. Chen, and J. Hu, “Kagome superconductors AV_3Sb_5 ($A = K, Rb, Cs$),” *arXiv preprint arXiv:2109.10809* (2021).
- [36] S.-Y. Yang, Y. Wang, B. R. Ortiz, D. Liu, J. Gayles, E. Derunova, R. Gonzalez-Hernandez, L. Šmejkal, Y. Chen, S. S. Parkin, *et al.*, “Giant, unconventional anomalous hall effect in the metallic frustrated magnet candidate, kv_3sb_5 ,” *Science advances* **6**, eabb6003 (2020).
- [37] A. Subedi, “Hexagonal-to-base-centered-orthorhombic 4Q charge density wave order in kagome metals KV_3Sb_5 , RbV_3Sb_5 , and CsV_3Sb_5 ,” *Physical Review Materials* **6**, 015001 (2022).
- [38] J. Zhao, W. Wu, Y. Wang, and S. A. Yang, “Electronic correlations in the normal state of the kagome superconductor KV_3Sb_5 ,” *Physical Review B* **103**, L241117 (2021).
- [39] H. Tan, Y. Liu, Z. Wang, and B. Yan, “Charge density waves and electronic properties of superconducting kagome metals,” *Physical review letters* **127**, 046401 (2021).
- [40] J.-F. Zhang, K. Liu, and Z.-Y. Lu, “First-principles study of the double dome superconductivity in the kagome material CsV_3Sb_5 under pressure,” *Physical Review B* **104**, 195130 (2021).
- [41] J.-G. Si, W.-J. Lu, Y.-P. Sun, P.-F. Liu, and B.-T. Wang, “Charge density wave and pressure-dependent superconductivity in the kagome metal CsV_3Sb_5 : A first-principles study,” *Physical Review B* **105**, 024517 (2022).
- [42] Z. Liu, M. Li, Q. Wang, G. Wang, C. Wen, K. Jiang, X. Lu, S. Yan, Y. Huang, D. Shen, J.-X. Yin, Z. Wang, Z. Yin, H. Lei, and S. Wang, “Orbital-selective Dirac fermions and extremely flat bands in frustrated kagome-lattice metal $CoSn$,” *Nature communications* **11**, 1 (2020).
- [43] M. Kang, S. Fang, L. Ye, H. C. Po, J. Denlinger, C. Jozwiak, A. Bostwick, E. Rotenberg, E. Kaxiras, J. G. Checkelsky, and R. Comin, “Topological flat bands in frustrated kagome lattice $CoSn$,” *Nature communications* **11**, 1 (2020).
- [44] X. Teng, J. S. Oh, H. Tan, L. Chen, J. Huang, B. Gao, J.-X. Yin, J.-H. Chu, M. Hashimoto, D. Lu, C. Jozwiak, A. Bostwick, E. Rotenberg, G. E. Granroth, B. Yan, R. J. Birgeneau, P. Dai, and M. Yi, “Intertwined magnetism and charge density wave order in kagome $FeGe$,” *arXiv preprint arXiv:2210.06653* (2022).
- [45] X. Teng, L. Chen, F. Ye, E. Rosenberg, Z. Liu, J.-X. Yin, Y.-X. Jiang, J. S. Oh, M. Z. Hasan, K. J. Neubauer, B. Gao, Y. Xie, M. Hashimoto, D. Lu, C. Jozwiak, A. Bostwick, E. Rotenberg, R. J. Birgeneau, J.-H. Chu, M. Yi, and P. Dai, “Discovery of charge density wave in a kagome lattice antiferromagnet,” *Nature* **609**, 490 (2022).
- [46] J.-X. Yin, Y.-X. Jiang, X. Teng, M. S. Hossain, S. Mardanya, T.-R. Chang, Z. Ye, G. Xu, M. M. Denner, T. Neupert, B. Lienhard, H.-B. Deng, C. Setty, Q. Si, G. Chang, Z. Guguchia, B. Gao, N. Shumiya, Q. Zhang, T. A. Cochran, D. Multer, M. Yi, P. Dai, and M. Z. Hasan, “Discovery of charge order and corresponding edge state in kagome magnet $FeGe$,” *Physical Review Letters* **129**, 166401 (2022).
- [47] C. Setty, C. A. Lane, L. Chen, H. Hu, J.-X. Zhu, and Q. Si, “Electron correlations and charge density wave in the topological kagome metal $FeGe$,” *arXiv preprint arXiv:2203.01930* (2022).
- [48] S. Shao, J.-X. Yin, I. Belopolski, J.-Y. You, T. Hou, H. Chen, Y.-X. Jiang, M. S. Hossain, M. Yahyavi, C.-H. Hsu, Y. Feng, A. Bansil, M. Z. Hasan, and G. Chang, “Charge density wave interaction in a Kagome-honeycomb antiferromagnet,” *arXiv preprint arXiv:2206.12033* (2022).
- [49] H. Miao, T. T. Zhang, H. X. Li, G. Fabbri, A. H. Said, R. Tartaglia, T. Yilmaz, E. Vescovo, S. Murakami, L. X. Feng, K. Jiang, X. L. Wu, A. F. Wang, S. Okamoto, Y. L. Wang, and H. N. Lee, “Charge Dimerization in Strongly Correlated Kagome Magnet $FeGe$,” *arXiv preprint arXiv:2210.06359* (2022).

- [50] T. Ohoyama, K. Kanematsu, and K. Yasukōchi, “A new intermetallic compound FeGe,” *Journal of the Physical Society of Japan* **18**, 589 (1963).
- [51] O. Beckman, K. Carrander, L. Lundgren, and M. Richardson, “Susceptibility measurements and magnetic ordering of hexagonal FeGe,” *Physica Scripta* **6**, 151 (1972).
- [52] L. Häggström, T. Ericsson, R. Wäppling, and E. Karlsson, “Mössbauer study of hexagonal fege,” *Physica Scripta* **11**, 55 (1975).
- [53] U. Gäfvert, L. Lundgren, B. Westerstrandh, and O. Beckman, “Crystalline anisotropy energy of uniaxial antiferromagnets evaluated from low field torque data,” *Journal of Physics and Chemistry of Solids* **38**, 1333 (1977).
- [54] J. Forsyth, C. Wilkinson, and P. Gardner, “The low-temperature magnetic structure of hexagonal FeGe,” *Journal of Physics F: Metal Physics* **8**, 2195 (1978).
- [55] J. Bernhard, B. Lebech, and O. Beckman, “Neutron diffraction studies of the low-temperature magnetic structure of hexagonal FeGe,” *Journal of Physics F: Metal Physics* **14**, 2379 (1984).
- [56] J. Bernhard, B. Lebech, and O. Beckman, “Magnetic phase diagram of hexagonal FeGe determined by neutron diffraction,” *Journal of Physics F: Metal Physics* **18**, 539 (1988).
- [57] H. Chen, Q. Niu, and A. H. MacDonald, “Anomalous hall effect arising from noncollinear antiferromagnetism,” *Physical review letters* **112**, 017205 (2014).
- [58] T. Suzuki, R. Chisnell, A. Devarakonda, Y.-T. Liu, W. Feng, D. Xiao, J. W. Lynn, and J. Checkelsky, “Large anomalous hall effect in a half-Heusler antiferromagnet,” *Nature Physics* **12**, 1119 (2016).
- [59] S. Nakatsuji, N. Kiyohara, and T. Higo, “Large anomalous hall effect in a non-collinear antiferromagnet at room temperature,” *Nature* **527**, 212 (2015).
- [60] F. Kekule, “Studies on aromatic compounds,” *Annalen der Chemie Und Pharmacial*, Leipzig **137**, 129 (1865).
- [61] A. I. Liechtenstein, M. Katsnelson, V. Antropov, and V. Gubanov, “Local spin density functional approach to the theory of exchange interactions in ferromagnetic metals and alloys,” *Journal of Magnetism and Magnetic Materials* **67**, 65 (1987).
- [62] X. Wan, Q. Yin, and S. Y. Savrasov, “Calculation of magnetic exchange interactions in mott-hubbard systems,” *Phys. Rev. Lett.* **97**, 266403 (2006).
- [63] X. Wan, T. A. Maier, and S. Y. Savrasov, “Calculated magnetic exchange interactions in high-temperature superconductors,” *Phys. Rev. B* **79**, 155114 (2009).
- [64] A. R. Mackintosh and O. K. Andersen, *Electrons at the Fermi surface* (1980).
- [65] M. Weinert, R. E. Watson, and J. W. Davenport, “Total-energy differences and eigenvalue sums,” *Phys. Rev. B* **32**, 2115 (1985).
- [66] I. Dzyaloshinsky, “A thermodynamic theory of weak ferromagnetism of antiferromagnetics,” *Journal of Physics and Chemistry of Solids* **4**, 241 (1958).
- [67] T. Moriya, “Anisotropic superexchange interaction and weak ferromagnetism,” *Physical Review* **120**, 91 (1960).
- [68] P. Blaha, K. Schwarz, G. K. H. Madsen, D. Kvasnicka, J. Luitz, *et al.*, “wien2k,” An augmented plane wave+local orbitals program for calculating crystal properties **60** (2001).
- [69] S. H. Vosko, L. Wilk, and M. Nusair, “Accurate spin-dependent electron liquid correlation energies for local spin density calculations: a critical analysis,” *Can. J. Phys.* **58**, 1200 (1980).
- [70] D. D. Koelling and B. N. Harmon, “A technique for relativistic spin-polarised calculations,” *J. Phys. C* **10**, 3107 (1977).
- [71] X. Wan, J. Dong, and S. Y. Savrasov, “Mechanism of magnetic exchange interactions in europium monochalcogenides,” *Physical Review B* **83**, 205201 (2011).
- [72] X. Wan, V. Ivanov, G. Resta, I. Leonov, and S. Y. Savrasov, “Exchange interactions and sensitivity of the Ni two-hole spin state to Hund’s coupling in doped NdNiO₂,” *Physical Review B* **103**, 075123 (2021).
- [73] D. Wang, X. Bo, F. Tang, and X. Wan, “Calculated magnetic exchange interactions in the Dirac magnon material Cu₃TeO₆,” *Phys. Rev. B* **99**, 035160 (2019).
- [74] N. Metropolis and S. Ulam, “The monte carlo method,” *J. Am. Stat. Assoc.* **44**, 335 (1949).
- [75] Z.-X. Shen, C. Su, and L. He, “High-throughput computation and structure prototype analysis for two-dimensional ferromagnetic materials,” *NPJ Comput. Mater.* **8**, 132 (2022).
- [76] K. Cao, G.-C. Guo, D. Vanderbilt, and L. He, “First-Principles Modeling of Multiferroic RMn₂O₅,” *Phys. Rev. Lett.* **103**, 257201 (2009).
- [77] P. Baral, N. Ahmed, J. Kumar, S. Nair, and R. Nath, “Synthesis and physical properties of spin-1 honeycomb lattice Pb₆Ni₉(TeO₆)₅,” *Journal of Alloys and Compounds* **711**, 568 (2017).
- [78] R. Chisnell, J. Helton, D. Freedman, D. Singh, R. Bewley, D. Nocera, and Y. Lee, “Topological magnon bands in a kagome lattice ferromagnet,” *Physical review letters* **115**, 147201 (2015).
- [79] T. Holstein and H. Primakoff, “Field dependence of the intrinsic domain magnetization of a ferromagnet,” *Physical Review* **58**, 1098 (1940).
- [80] D. Wang, J. Yu, F. Tang, Y. Li, and X. Wan, “Determination of the Range of Magnetic Interactions from the Relations between Magnon Eigenvalues at High-Symmetry κ Points,” *Chinese Physics Letters* **38**, 117101 (2021).
- [81] C. J. Bradley and A. P. Cracknell, *The Mathematical Theory of Symmetry in Solids: Representation Theory for Point Groups and Space Groups* (Oxford University Press, Oxford, 1972).